MAX IV Beamline Review Report

# MAXPEEM

June 2023

# MAXPEEM Beamline Review Report

The MAXPEEM beamline team

Spring 2023

# 1 Introduction

MAXPEEM is a soft X-ray (30 – 1200 eV) beamline connected to the 1.5 GeV storage ring at MAX IV Laboratory; it hosts an Elmitec-manufactured, aberration-corrected Spectroscopic PhotoElectron and Low Energy Electron Microscope (AC-SPELEEM, also referred to as the spectroscopic microscopy end station here) that is designed such that X-rays impinge the sample at normal incidence [1]. This geometry results in more effective sample illumination and eliminates shadowing effects, a unique feature compared to peer beamlines designed for a grazing incidence geometry. In addition, it favors studies with out-of-plane magnetic moments in XMCD and in-plane magnetic moments in XMLD experiments.

The SPELEEM instrument is unique in that it provides unified and simple access to a number of complementary contrast mechanisms with a spatial resolution in the nanometer range. Surface imaging techniques with structural, chemical, electronic, and magnetic contrasts can be used on the same sample, which is valuable for materials science studies which seek to elucidate structure-property-function relationships. Consequently, the beamline is popular in a wide range of disciplines, such as materials science, nano-science, heterogeneous catalysis, corrosion science, polymer science, and more.

SPELEEM also has the advantage of having a large dynamic field of view of up to ~100 microns, thereby facilitating easy access to the structure not only at the nanometer scale but at the micrometer scale as well. Finally, as the detection in SPELEEM is performed at up to 5 frames per second (limited by the camera), monitoring of real-time dynamical processes is possible.

We believe the following are the overall strengths of MAXPEEM:

- Ability to probe different portions of electronic structure (valence band and core levels): beamline offers a range of photon energies from ultraviolet to soft X-ray
- Multiple excitation sources for both online and offline use: ultraviolet/X-rays (beamline), electron-beam and mercury lamp (local)
- Real space and k-space imaging in one instrument
- Spatial resolution down to a few nanometers
- High photon flux and high resolution gratings offer both high quality imaging and spectroscopy
- Out-of-plane magnetization: dynamic and static, due to normal incidence configuration

The SPELEEM end station was transferred from the former MAX-lab facility, where it served as a secondary end station on the I311 beamline since 2007 [2]. Hence, the user community is well-developed and strong, which is reflected in the continuous output of publications from I311-PEEM till now. The microscope has been upgraded and improved since the transfer, where the aberration correction is the most impactful on the instrument itself (spatial resolution improvement by an order of magnitude and improvement in transmission by a similar factor). The change from a linearly polarizing undulator to an elliptically polarizing undulator (EPU) upon transfer to the MAX IV facility is another major upgrade, which has opened up the doors to the magnetic materials research community.

## 1.1 Charge questions

- The MAXPEEM beamline is designed for two branch lines and one is currently utilized. Does the committee agree with the suggestions we have put forth in section 6.3 for developing the second branch line?
- Is MAXPEEM currently competitive with similar facilities worldwide?
- Are our suggested improvements/developments in line with maintaining/improving our competitiveness?
- Does the size and composition of our user community, and its research output (rate and impact) match the beamline's strengths?
- What strategy and framework is appropriate for proprietary research at MAXPEEM?
- Is staffing at MAXPEEM in line with reaching development goals and scientific output?

# 2 Technical description

## 2.1 Beamline design

The MAXPEEM beamline is designed for two branch lines; one hosts the SPELEEM microscope, whereas the instrument(s) for the second branch is (are) still under consideration. The beamline geometry is determined primarily by the focusing needs set by the microscope. To achieve the highest spatial resolution in XPEEM mode one needs to focus the beam down to a spot of a few micrometers (µm). On the other hand, for some experiments, much larger fields of view, up to 50 or even 100 µm, are necessary. For the majority of experiments, we expect the optimal beam spot size to be around 15-20 µm. This tradeoff provides sufficient photon flux for high spatial resolution measurements. Therefore, the design goals were set as follows:

- Minimum number of optical elements in the beamline, to maximize photon flux
- Focussed beam spot size on sample is ca. 15 x 15 µm
- Defocussing up to 50 - 60 µm for overview images shall be possible, easy and fast
- Illumination area at sample shall match the field of view for imaging with very high spatial resolution (to limit resolution-degrading space charge effects).

The last goal can be achieved only by reducing the size of the source at the exit slit. Ideally, at high magnifications for XPEEM the spot size should match the field of view, which can be as small as 2.5 µm. If the illuminated spot size will be much larger than the field of view, it may generate excessive space charge and blur the image. However, accurate calculation of the space charge effect is a difficult task, depending on the time structure of the ring, photon intensity and energy, illumination area etc. That is why it is nontrivial to specify the minimal spot size, for which the resolution is not yet limited by the space charge effect.

The optical beamline design was primarily developed by Alexei Preobrajenski, and calculated using the XRT software package written by Konstantin Klementiev (both employed at MAX IV) [3]. The design had to accommodate the monochromator used at the MAX-lab beamline I311, which previously hosted the SPELEEM. Therefore, it had to solve adequately the heat load issues, and provide high energy resolution at relatively high flux within a broad energy range and with an option of both focussed and defocussed beam on sample. In the following sections we will describe the source and the optics of

MAXPEEM and illustrate the beamline's present performance. For in-depth reading about the design principles and solutions we refer the reader to the "Detailed design report" (DDR) [4]. Note that the document was produced in 2015 and some aspects of the design may have changed.

### *2.1.1* 1.5 GeV ring and insertion device

The MAX IV 1.5 GeV electron storage ring is based on a compact double-bend achromat lattice and produces bright soft X-ray and ultraviolet (UV) radiation [5]. With its circumference of 96 m and 12 achromat sections, it uses similar magnet technology as the 3 GeV ring. At the center of the MAXPEEM straight section, the RMS values of the e-beam size and divergence are 184 (h) x 13 (v) µm and 33 (h) x 5 (v) µrad, respectively. The 1.5 GeV ring operates today at its designed (and maximum) current of 500 mA with a top-up interval of 10 min.

The light source for the MAXPEEM beamline is an elliptically polarizing undulator (EPU) of Apple-II type [6]. The insertion device is called EPU58 due to its period length of 58 mm and has 42 periods. The maximum radiated power is 1.46 kW (planar phase, 500 mA ring current). Undulator parameters for a variety of operation modes are summarized in Table 1. The estimated maximum flux into the beamline is ≥ $10^{15}$ photons/sec/0.1% bandwidth. The undulator was tuned and characterized in a magnetic bench prior to installation and after installation into the ring. The fundamental harmonics (linearly polarized light) covers the photon energy range of 30 - 350 eV; Figure 1 shows calculated (horizontally polarized) photon flux for the odd harmonics generated by the software Spectra [7]. The energy range was chosen based on the science that was prevalent during the time of MAX-lab, where valence band studies using spatially resolved ARPES on 2D materials like graphene, and using the shallow core levels of III-V nanowires, provided the main tools for looking at their electronic band structure. Consequently, the upper bound of the fundamental harmonic is less ideal for magnetism studies, which have to be conducted using the higher orders. The 1.5 GeV ring is in this respect, less ideal for magnetic studies, which are better hosted at the 3 GeV ring. The choice was therefore made to favour the lower energy range. When the EPU58 is tuned to produce circularly polarized light only the first harmonic has intensity on the optical axis and covers the photon energy range of 30-300 eV. For higher harmonics, the undulator must be tuned to produce elliptically polarized light with degree of circular polarization less than 100%. The undulator also works in the inclined mode, and it can produce a linearly polarized light at an arbitrary azimuth angle, i.e., from –90° to +90°.

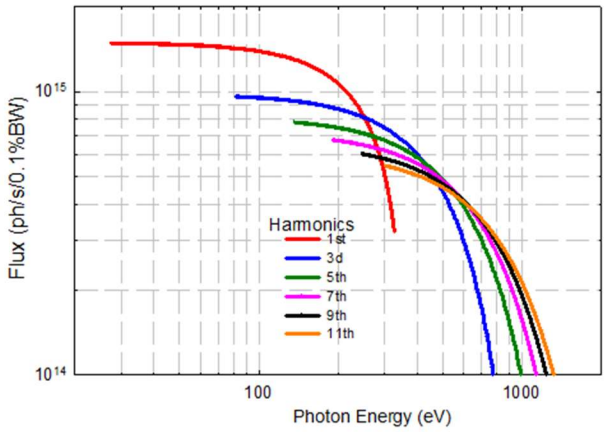


*Figure 1. Flux of horizontally polarized photons in the odd harmonics from the EPU58 undulator placed at the MAX IV 1.5 GeV storage ring filled with 500 mA and using a 0.1%BW monochromatization.*

| | Horizontal mode | Helical mode | Inclined mode | Vertical mode |
|---|---|---|---|---|
| Phase (mm) | 0 | 17.38 | 16.01 | 29 |
| Vert. field, T | 0. 9164 | 0.5385 | 0.3854 | 0 |
| K-value | 4.964 | 2.917 | 2.088 | 3.610 |
| hν (1st harm., eV) | 30 | 40 | 70 | 50 |
| Power (kW) | 1.46 | 1.01 | 0.5 | 0.77 |

*Table 1. EPU58 parameters for specific modes of operation.*

### *2.1.2* Beamline optics

As a consequence of the normal incidence light geometry of the end station, there is a limitation on the length of the refocusing optics exit arm, which is about 900 mm and is determined by the geometry of the existing XPEEM instrument. Given this limitation, there exists two possibilities for the refocusing optics to meet the aforementioned design goals. The first option is to use a more traditional solution with a KB pair of plane-elliptical mirrors. The second option is to use a single ellipsoidal mirror focusing in both directions. Choosing between these two options, we decided to prefer the scheme with a single-mirror refocusing (M4), due to its simplicity, higher flux, purely horizontal deflection and lower costs.

Diffraction effects are not included explicitly in the ray-tracing calculations (performed with the XRT code, however we are aware they can be a limiting factor for the spot size at the lowest photon energies (around 30 eV) [3]. Some modelling of diffraction effects has been done using the RAY program.

The optical layout of the beamline is shown schematically in Figure 2. After passing the frontend, the EPU radiation is deflected horizontally (by 4°) and collimated vertically by a water-cooled cylindrical mirror M1 at 15000 mm after the EPU source. The size of M1 determines the acceptance of the beamline, which was selected to be 0.80 mrad x 1.36 mrad (h x v). Horizontal acceptance is chosen to be relatively large, 8σ (σ = 0.1 mrad is the standard deviation of the angular opening of the 1st undulator harmonic at the lowest photon energy of 30 eV). For accepting 99.7% of the monochromatic radiation the fan of 6σ would be sufficient, but even larger horizontal acceptance makes the thermally induced deformation smoother in the central area, which is irradiated by the light of interest. The need for full illumination of M1 determines its length to be 350 mm. The high vertical acceptance follows from the fact that it is difficult to make a mirror narrower than 20 mm, and at a distance of 15000 mm this corresponds to 1.36 mrad. The water-cooled baffles in front of the monochromator can reduce both horizontal and vertical acceptance further.

The monochromator is the Zeiss SX-700 plane grating monochromator (PGM) from the former beamline I311 at MAX-lab. With this scheme, the beam is parallel to the floor (i.e., easier operation and exchange of end stations) and the exit slit is fixed in space for different $c_{ff}$ values (the PGM parameter $c_{ff}$ is a cosine ratio of the diffracted and incident angles and may be varied for better suppression of the higher diffraction orders). Before installing at MAXPEEM, our SX-700 was equipped with new stepper motors, drives and gear boxes; it also was integrated in the standard MAX IV control system and calibrated. The optical elements inside the monochromator are the plane mirror (M2) and the plane gratings (PG, up to three). The old optical elements have been preserved for now; two 1221 l/mm gratings with different blaze angles provide higher energy resolution and photon energy range, and a 300 l/mm grating which is used for flux-hungry experiments below 600 eV. A new 650 l/mm grating has arrived and awaits installation (one 1221l/mm, with high blaze angle will be removed). The

characteristics of the gratings are summarized in Table 2. With the new 650 l/mm grating covering both low-E/high-E range at good resolution, it will become the main grating.

| | Groove density (l/mm) | Optical area (mm) | Substrate | Coating | Blaze angle (°) |
|---|---|---|---|---|---|
| PG1 (hi-blaze) | 1221 | 110 x 30 | Si | Au | 1.3 |
| PG2 (low-blaze) | 1221 | 110 x 30 | Si | Au | 1.03 |
| PG3 | 300 | 110 x 30 | Si | Au | ** |
| PG4* | 650 | 110 x 30 | Si | Au | 1.0 |

*Table 2. Characteristics of the gratings installed at MAXPEEM. PG1 will be removed when PG4 is installed.*

The dispersed radiation from the grating is focused both vertically and horizontally at the exit slit by a toroidal focusing mirror (M3). This mirror has to accept the fan of 6σ (because heat deformations are not as important as for M1), setting the length of M3 to 320 mm. After the exit slit, a gas cell is mounted for monitoring beamline resolution with the spectra of gases (e.g. He, $N_2$ and Ne). Motorized diagnostic sections along the branch allow us to measure 1) the profile of the beam at M4 with YAG screens and cameras and 2) the total photon flux with photodiodes. These tools were used extensively for the beamline alignment and are still used occasionally for the performance checks. Particularly important for regular user operation is the $I_0$ section placed just before M4. We use a gold mesh with an opening (slit for the beam) as an $I_0$ sensor (excluding the carbon edge, see upgrades). Other diagnostic tools are phosphorus screens and cameras on the 1) beam-defining apertures before the PGM, 2) beam-defining apertures before M3 and M4, and 3) exit slit. Finally, we can monitor the drain current from the M4 mirror.

The final refocusing is accomplished by a single ellipsoidal mirror (M4) deflecting the beam horizontally. The length of M4 is set to 260 mm accepting 85% of intensity at 30 eV and more at higher energies (longer M4 would give slightly more flux at low energies but it would also increase the level of slope errors, the price, and require larger and more expensive vessel and mechanics). The image at the exit slit plane is demagnified by a factor of 10 at the sample position. The grazing incidence angles for M1, M3 and M4 are all 2°. The spot size at the sample position in the XPEEM branch is around 15(h) x 15(v) $\mu m^2$ (with 0.15 mm exit slit opening vertically and horizontally) and can be reduced to approximately 12(h) x 4(v) $\mu m^2$ or increased by defocusing beyond 30 µm (yaw rotation of M4). The relatively large horizontal spot size results from the expected tangential slope errors on M4. Basic parameters of optical components and their positions are summarized in Table 2 (mirrors and slits) and in Table 3 (gratings). In summer 2023, a new grating (650l/mm) will be installed covering a significant part of the energy spectrum (50 - 900eV).

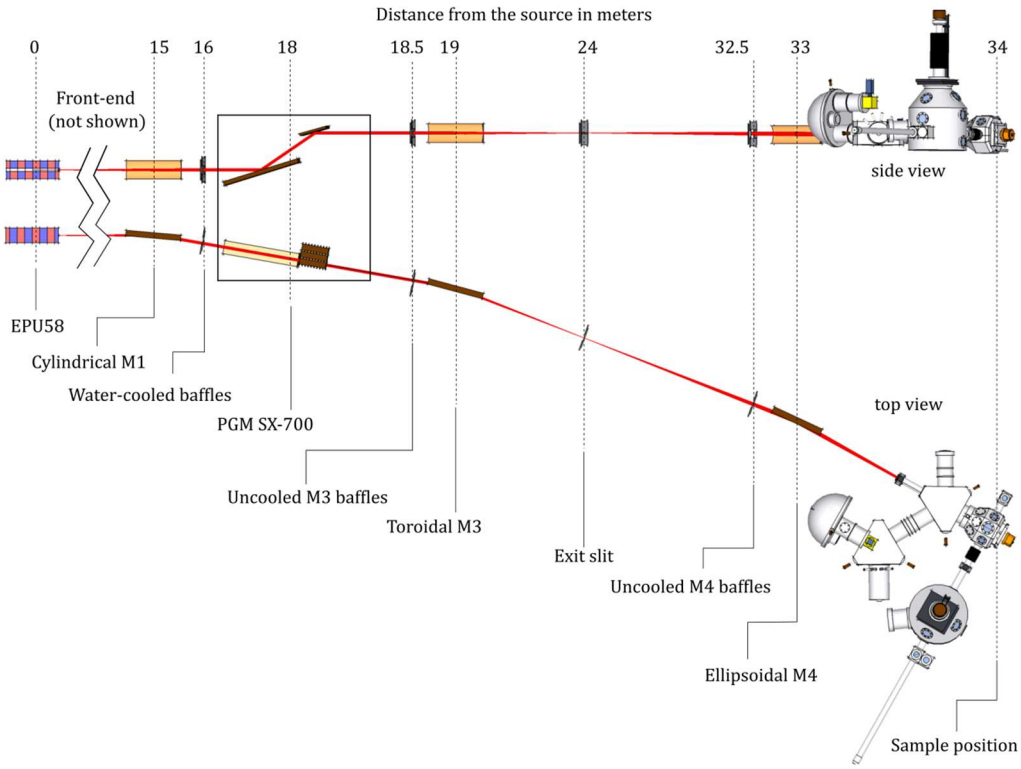


*Figure 2. Schematic of the optical layout of the MAXPEEM beamline. The horizontal view is shown at the top and the top view is shown at the bottom. A single refocusing mirror M4 is present. Distances are given in meters.*

| | M1 | M2 | M3 | Slit S1 | M4 |
|---|---|---|---|---|---|
| Shape | cylindrical | plane | toroidal | rectangle | ellipsoidal |
| Deflection | horizontal | vertical | horizontal | - | horizontal |
| Distance (mm) | 15000 | var. | 19000 | 25000 | 34000 |
| Incidence angle (°) | 2 | 1 – 13 | 2 | - | 2 |
| Geom. Size (mm) | 370x40x60 | 640x40x110 | 340x40x40 | | 280x40x40 |
| Opt. area (mm) | 350x20 | 640x40 | 320x20 | | 260x20 |
| Substrate material | Si | Si | Si | - | Zerodur |
| Coating material | Au | Au | Au | - | Au |
| Roughness (Å) | 3 | 3 | 3 | - | 3 |
| Slope error (arcsec) | 0.3 / 1 | 0.1 / 0.1 | 0.3 / 1 | - | 0.75(*) / 5 |
| Sag. entrance (mm) | 15000 | - | ∞ | - | 9000 |
| Sag. exit (mm) | ∞ | - | 6000 | - | 900 |
| Tang. entrance (mm) | - | - | 19000 | - | 9000 |
| Tang. exit (mm) | - | - | 6000 | - | 900 |
| Parameters | r = 1046.98 mm<br>R = ∞ | | r = 418.79 mm<br>R = 261321.8 mm | Width<br>0…4 mm<br>Height<br>0…1 mm | A = 4950<br>B = 99.326<br>$Y_0$ = -4047.533<br>$Z_0$ = 172.753 |

*Table 3. Parameters of key optical elements for the XPEEM branch of the MAXPEEM beamline. All lengths are in millimeters. RMS slope errors are represented as tangential / sagittal.*

**) The best guaranteed tangential slope error on M4.*

| | Dimensions (l, w, h) (mm) | Optical area (l, w) (mm) | Substr. | Coating | Slope errors (arcsec) | Roughness (Å) | Blaze angle (°) |
|---|---|---|---|---|---|---|---|
| PG1, 300 l/mm | 120 x 40 x 25 | 110 x 30 | Si | Au | 0.1 / 0.1 | 5 | 0.4 |
| PG2, 1200 l/mm | 120 x 40 x 25 | 110 x 30 | Si | Au | 0.1 / 0.1 | 5 | 1.0 |

*Table 4. Parameters of the plane gratings currently in use at MAXPEEM.*

### *2.1.3* Measured versus calculated performance: insertion device and beamline

Insertion device

The actual performance of the EPU58 is in very good agreement with earlier simulations (Figure 3); a small energy shift of 3.5 eV exists due to imperfect mutual alignment of the insertion device and the beamline [7]. The measured undulator spectrum of the first harmonic contains all of the interference fringes generated by the simulation (inset to Figure 3).

In 2022, we performed extensive complementary simulations of our undulator spectrum. We used the software package Radia, which performs magnetostatic calculations and outputs the B field profile along the two directions perpendicular to the axis of the undulator [8]. The magnetic fields were used as input for the updated program Spectra, which numerically evaluates the characteristics of radiation emitted from synchrotron radiation sources [9]. The calculated parameters of interest to us are the photon flux and the four Stokes parameters.

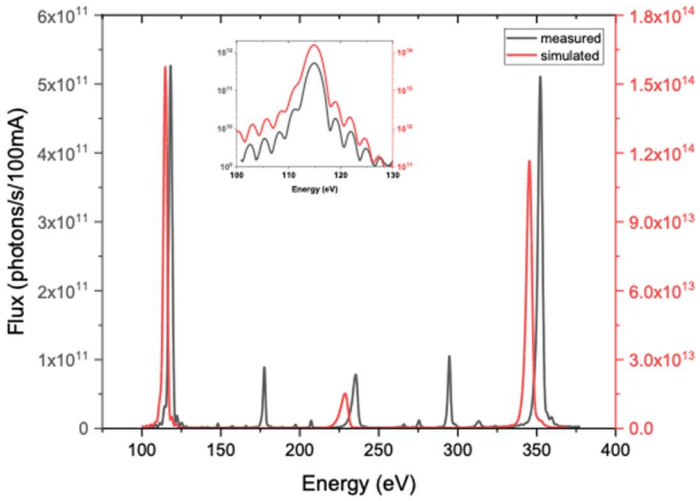


*Figure 3. Simulated and measured undulator spectra in the planar mode for an undulator gap of 30 mm. The beamline opening is 0.1 mrad. The monochromator grating features 1221 l/mm. The inset shows the agreement of the simulated and measured spectra for the first harmonic at 115 eV (note the logarithmic scale on the y-axis), where the small energy shift of 3.5 eV has been corrected. The experimental undulator spectrum has been measured right after the exit slit of the beamline.*

The results of our simulations were used as a guide for a beamline commissioning using a soft x-ray polarimeter, where we confirmed the predictions of our model. As an example, you can see predictions for the inclination angles of all (gap, phase) space at photon energy of 708 eV (see Figure 4(a)). The measured spectra at specific (gap, phase) pairs on the constant contours validated our model's predictions for the inclination angle. Additionally, after the undulators' commissioning and

simulation, we have since 2022 a lookup table with known circular polarisation percentage for circularly polarized light at the energy region above 500 eV (Figure 5)

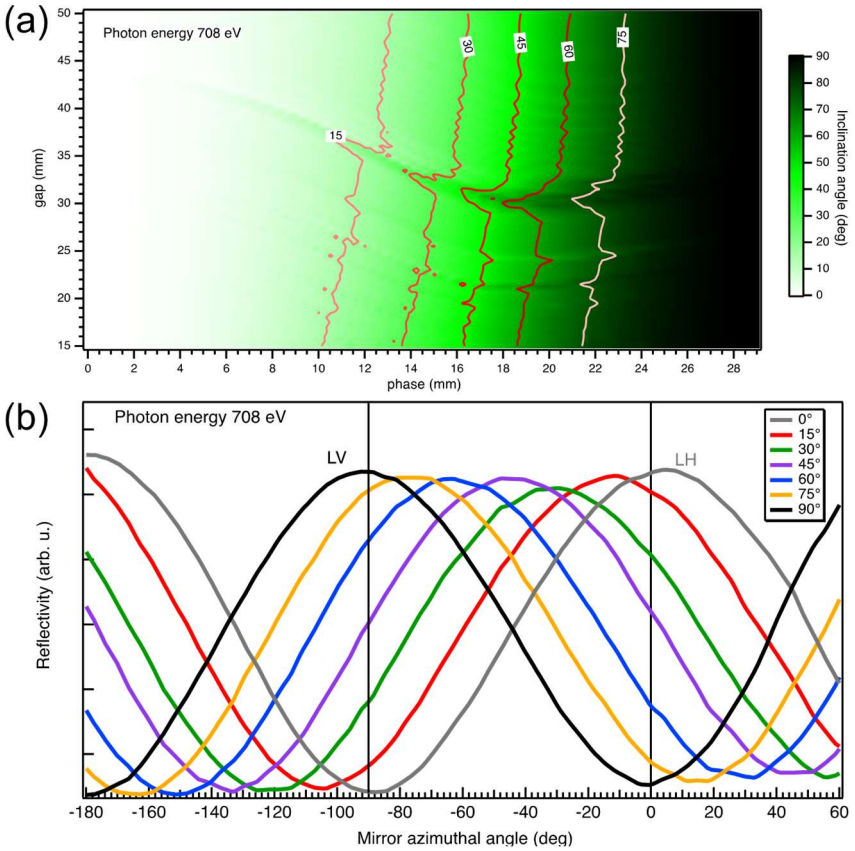


*Figure 4. (a) Prediction of the inclination angle for the whole (gap, phase) space of EPU58 at 708 eV photon energy. The contours represent (gap, phase) pairs with constant inclination angle indicated by the respective label (b) Reflectivity measurements with the X-ray polarimeter at selected points in gap/phases phase space where the third harmonic (now shown in (a)) intersects the constant angle contours in (a).*

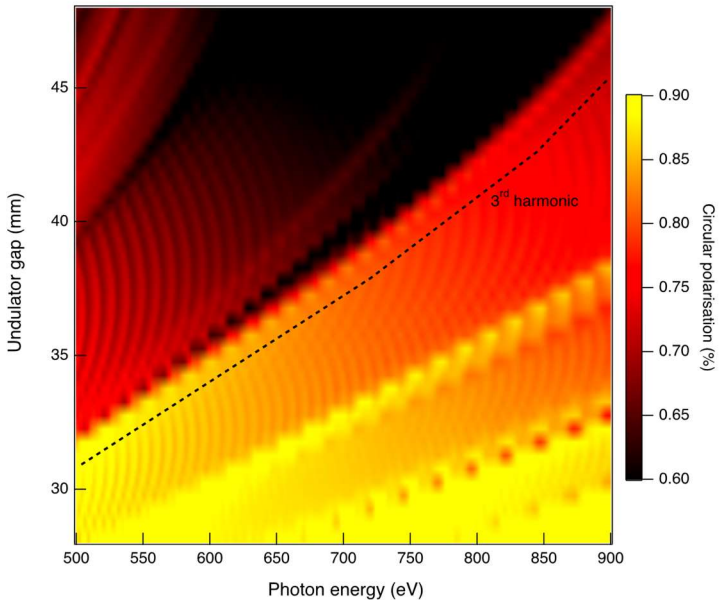


*Figure 5. Degree of circulator polarization of the third harmonic generated by EPU58. The dashed line represents the trajectory in gap/phase space of the third harmonic, which is set by the control software of our beamline.*

Beamline

The measured and calculated optimal spot size is presented in Figure 6. The beamline's photon flux within the main energy range, 30 to 545 eV for the low-density (LD) grating (300 l/mm) and 70 to 1100 eV for the high-density (HD) grating (1221 l/mm) is shown in Figure 7. The photon energy resolution of the beamline was measured by studying the absorption spectrum of molecular nitrogen recorded with a gas cell. The ion yield spectrum at the $N_{1s}\rightarrow 1\pi_g^*$ excitation region is shown in the inset of Figure 7. The spectrum has been measured with the HD grating at a small vertical exit slit (≈20 µm). The instrumental broadening was estimated by calculating the intensities of the first valley in the spectrum and the third peak [10]. A Gaussian broadening of 60 meV, at 400 eV photon energy gives the resolving power of the monochromator about 7000 for the HD grating. The number for the LD grating is 3 times lower but still sufficient for most of the measurements since it matches the energy resolution of the microscope.

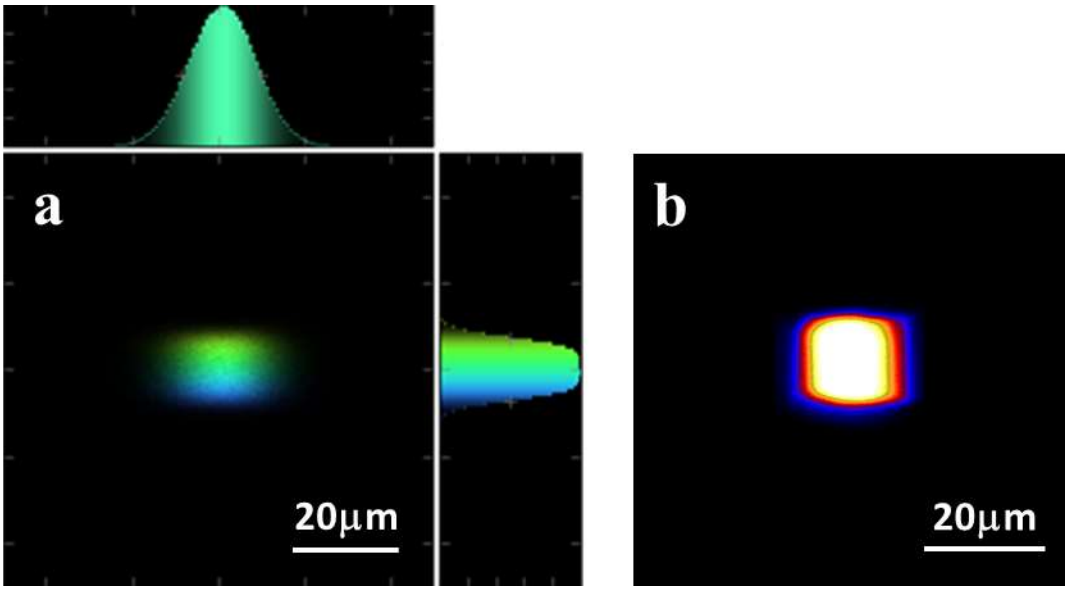


*Figure 6. Beam profile at the sample position. (a) Simulation of the beam profile performed with the X-ray tracing software (K. Klementiev), photon energy of 40 eV, energy slit setting of 150 x 150 µm² (h x v). The color code is the energy dispersion that scales with the photon energy. It is ± 7 meV at 40 eV photon energy. (b) Experimental beam profile in the photoelectron microscope at 43 eV photon energy. The beamline energy slit is 150 x 65 µm² and the signal originates from secondary photoelectrons discriminated by the energy analyser of the microscope (energy window of 0.2 eV).*

The energy scale is calibrated using the Fermi level positions measured from a clean gold sample. The accuracy and reproducibility of the energy scale is below 100 meV (at 500 eV) but increases up to 500 meV (at 1500 eV). The energy can be scanned in the standard step-by-step regime for XAS & XMCD measurements.

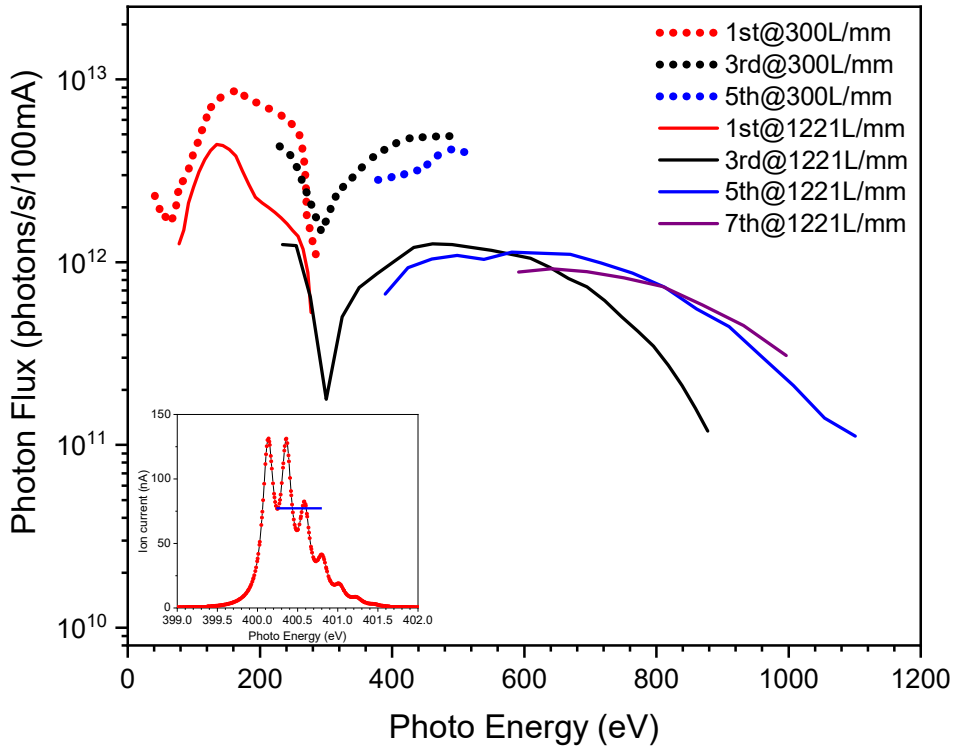


*Figure 7. Photon flux measured after the exit slit, for two monochromator gratings, 300 l/mm and 1221 l/mm. The beamline opening is 0.15 mrad and the energy slit is (h x v) 150 x 300 μm². The inset shows the ion yield spectrum for the nitrogen 1s absorption edge of nitrogen gas.*

## 2.2 Spectroscopic microscopy end station

### *2.2.1* Overview

The end station at MAXPEEM is a state-of-the-art aberration-corrected Spectroscopic PhotoElectron and Low Energy Electron Microscope (AC-SPELEEM) from Elmitec GmbH. The microscope was initially installed at the former beamline I311 of the old MAX II ring in 2014 and was moved to the MAX IV facility in 2016. Since its installation, the microscope has undergone a series of upgrades, both in hardware and software, which have kept it at the forefront of PEEM stations worldwide.

The schematic diagram of the AC-SPELEEM endstation is shown in Figure 8. It comprises four distinct vacuum sections: an analysis chamber, a column chamber, a preparation chamber, and a load-lock.

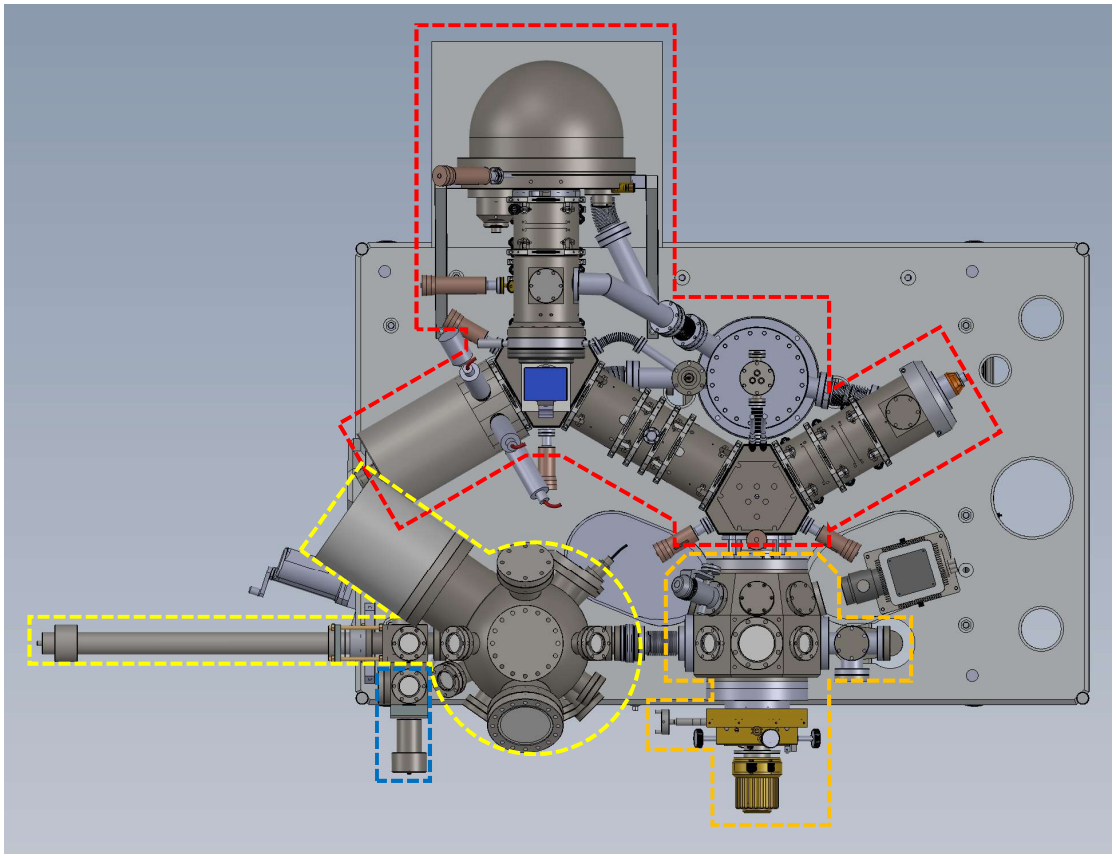

*Figure 8. A schematic diagram of the AC-SPELEEM endstation (top view). Four vacuum-separated chambers are highlighted, including the main chamber (orange), the column chamber (red), the preparation chamber (yellow) and the load-lock (blue). Note that both the electron energy analyzer and the camera have been upgraded.*

The analysis chamber, also known as the main chamber, houses the objective lens and sample stage, where the sample is analyzed with multiple sources, including the electron beam, UV light, and X-rays. In this chamber, live imaging is possible not only at varying temperatures, from 89 K to 1600 K, but also under varied external conditions, i.e. magnetic field, electric potential or current and material/gas deposition. The present manual manipulator will be upgraded to a fully motor-driven one this summer.

The column chamber includes the rest of the electron optics of the microscope, which are two separators, the illumination column, the intermediate column, the imaging column, and the camera. The electron energy analyzer in the imaging column has recently been upgraded from R100 to R200. Consequently, a twofold improvement in energy resolution is achievable (see below in Section 2.2.3).

The preparation chamber is a versatile, large ancillary chamber that serves a multitude of purposes, such as preparing samples and accommodating other characterization instruments. . It has in situ sample preparation facilities including material deposition, LEED measurements, gas dosing, sputtering and annealing up to 2000 K.

The load-lock is a compact design that has proven to be highly reliable for fast sample loading without compromising the ultra-high vacuum conditions of the other chambers. It takes about 20 to 30 minutes to pump down the load-lock before a sample can be transferred into the preparation chamber.

### *2.2.2* Operation modes

An (AC-SPELEEM) is a complementary instrument and has a plethora of imaging modes. In the LEEM mode, a beam of low energy electrons are impinging on the surface and an image of reflected or diffracted electrons yields structural information on the nanometer scale. The high flux and brilliance of synchrotron light along with its tunability and polarizability allows implementation of laterally resolved applications of the most important spectroscopic techniques. One of them, X-ray photoemission electron microscopy (XPEEM) fully exploits the many advantages of synchrotron radiation and provides unprecedented opportunities to image surfaces and thin films with chemical and magnetic sensitivity.

Some of the most important imaging modes of the microscope are listed below:

- X-ray Photoemission Electron Microscopy (XPEEM) – energy filtered imaging. The technique can be used for slow secondary electrons (utilizing a work function contrast) as well as for core-level electrons characteristic for the studied material. This allows performing elemental/chemical mapping.

- X-ray Magnetic Circular (Linear) Dichroism (XMCD, XMLD). Utilizing the circular polarization of the photon beam and magnetic circular dichroism effect (MCD), the imaging of magnetic domains in ferromagnets is possible on the nanometer scale (XPEEM-XMCD). Using the linear polarization of the photon beam and magnetic linear dichroism (MLD) effect, magnetic domains in antiferromagnets can also be imaged on the same scale.

- Micro-X-ray Photoemission Spectroscopy (micro-XPS). Photoelectron spectroscopy from extremely small areas down to a fraction of a micron. High flux on the samples allows both high spatial and high energy resolution.

- Micro-X-ray Absorption Spectroscopy (XAS). The microscope images the secondary electron emission at fixed kinetic energy as a function of the photon energy. In combination with linear and circular dichroism, XPEEM has become the main tool for imaging the magnetic state of surfaces, thin films, and buried interfaces.

- PhotoElectronDiffraction( PED). The intensity of a core level line as a function of energy and emission angle is measured. The technique can provide spatially resolved information on the surface crystallographic structure and is therefore complementary to LEED and STM. If the valence band electrons form a diffraction pattern, the band- and Fermi surface mapping in the full cone become possible (micro-ARPES).

- Low Energy Electron Microscopy (LEEM). This is the most powerful technique for imaging the morphology of crystalline surfaces. Several contrast mechanisms (including Dark Field Imaging) allow the determination of the lateral dimensions of regions with a given crystal structure, the thickness distribution of thin overlayers with monolayer resolution, the imaging of monoatomic surface steps and other morphological features.

- Micro-Low Energy Electron Diffraction (micro-LEED). By simply switching one lens and removing the contrast aperture the LEED pattern of the imaged area can be obtained. The imaged area can be as small as 100 nm, so the diffraction pattern from such a small area can be obtained.

### *2.2.3* Performance of AC-SPELEEM

Figure 9 presents the results of the on-site acceptance test for our AC-SPELEEM, conducted at the I311 beamline of the former Max-Lab in 2014. The average resolutions are specified for each image. A notable enhancement in both resolution and contrast is evident when the aberration corrector is activated. It's important to highlight a significant space charge effect that occurs in the mirror column, due to the deceleration of electrons at that point. This effect results in a blurring of the image. To mitigate this, in the XPEEM image illustrated in Figure 10, we inserted a 50µm select area aperture. This adjustment helped minimize the space charge effect by eliminating the photoelectrons outside the Field of View (FoV), thereby enhancing the resolution. A detailed investigation into the space charge effects within our AC-SPELEEM will be detailed in Section 4.6.

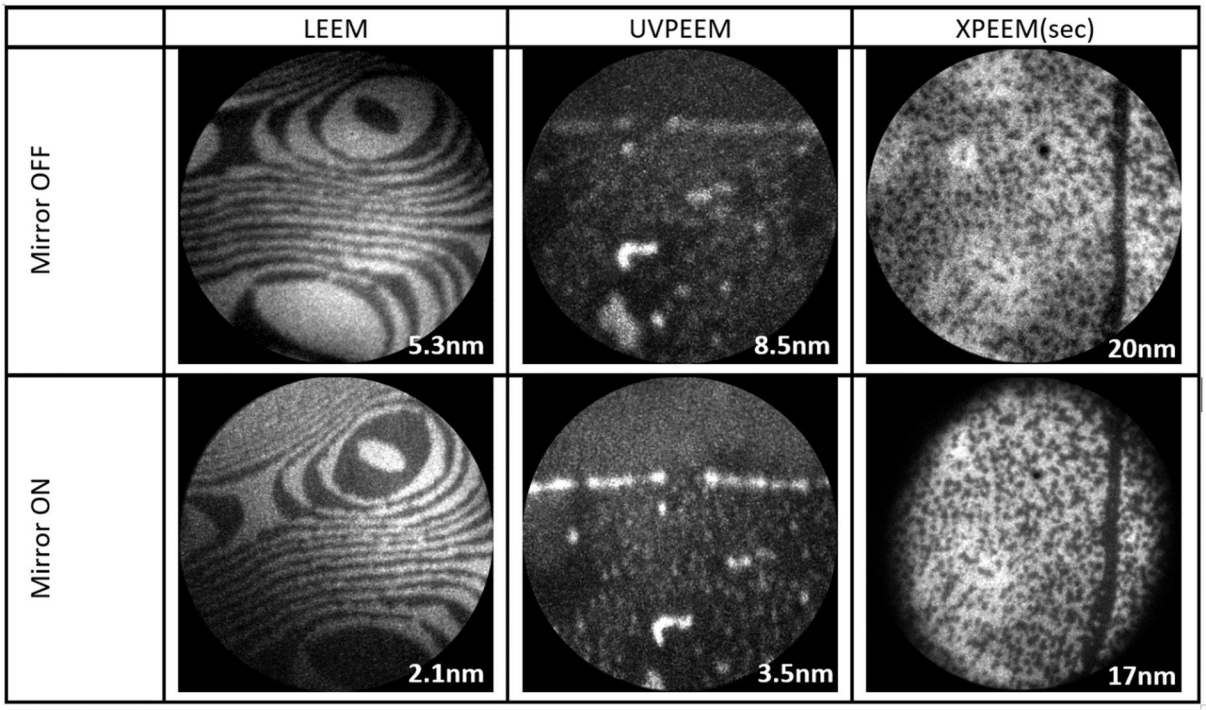


*Figure 9. LEEM, UVPEEM and XPEEM secondary images with aberration correction mirror kept OFF (upper row) and ON (lower row) recorded at the site acceptance test in 2014 at Beamline I311 of the former Max-lab. The FoV of LEEM and UVPEEM is 750 nm and the FoV of XPEEM is 2.5 µm. LEEM images were taken from a Si(001) sample with darkfield images of (1X2) and (2X1) terraces using STV=4.3 eV. UV-PEEM images were taken from a Graphene/Au/SiC(0001) sample using STV=0 eV. XPEEM images were taken from a graphene/Ge/SiC(0001) sample using STV=3 eV and a photon energy= 133 eV. For both graphene samples, there are n- and p-doped areas with different amounts of Au or Ge at interfaces. The contrast aperture of 30µm/40µm and energy slit of 25µm were used when taking the images. For the last XPEEM image, a select area aperture of 50µm was used.*

At high magnifications the stable environment, mechanical noises, temperature and electronic stability are the key factors for a good microscope performance. It means that a short acquisition time and subsequent drift correction of the stack of images can markedly improve the image quality. By employing this method, in Figure 10, we have demonstrated a spatial resolution of 10 nm in the XPEEM mode provided space charge effects are very carefully controlled.

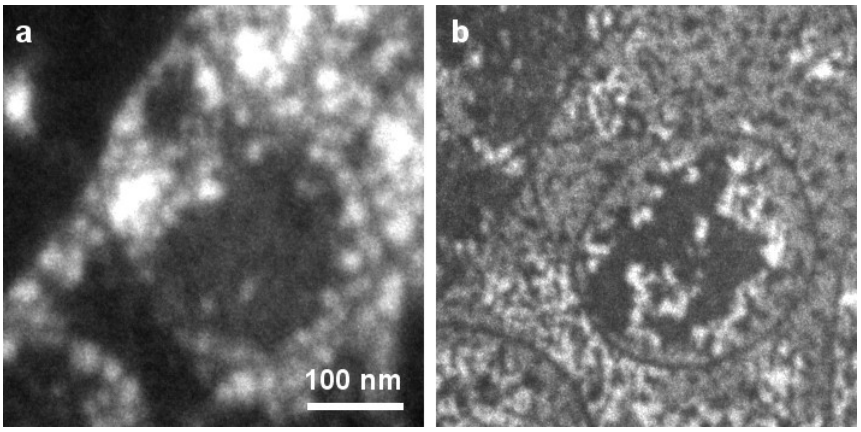


*Figure 10. High-resolution secondary XPEEM (a) and LEEM (b) images of Sn/SnOx intercalated graphene. For the XPEEM image, every single frame was acquired with 1 sec exposure time in the stack of 185 images. Before integration, the images in the stack were drift-corrected. For the LEEM image, the image was integrated from eight frames with 1 sec exposure time without drift correction (n.b. the single step is clearly visible in both images).*

In a bid to improve performance, we upgraded the electron energy analyzer from R100 to R200 last summer. A preliminary energy resolution test was recently conducted. The findings revealed an energy resolution better than 60 meV in µ-XPS mode and 120 meV in µ-ARPES mode, aligning with the specified expectations (Figure 11).

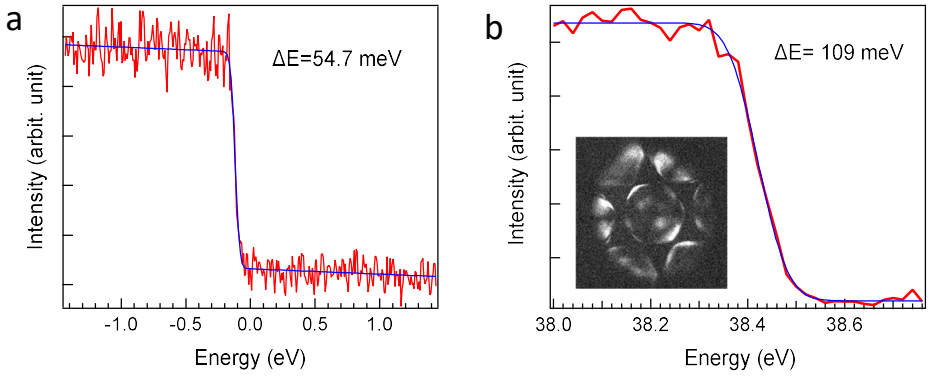


*Figure 11. Energy resolution measurements. µ-XPS (a) and µ-ARPES (b) measurements of the Fermi level of Ag(111) at T=100K. Photon energy is 43 eV. The inset in b) is a µ-ARPES image recorded at 0.52 eV below the Fermi surface.*

### *2.2.4* Sample holders and transfer system

Figure 12 shows a standard sample holder (cartridge) used in AC-SPELEEM. The sample is fixed into the sample holder with a Mo cap after gentle tightening of four symmetrically placed M2 screws. In both the preparation chamber and the main chamber, the sample can be heated to 400 °C (radiative heating) with a filament built in the sample holder or be heated to even higher temperatures (1300-1500 °C) by e-beam bombardment. For rough temperature measurement, there is a type-C thermocouple (W5%Re/W26%Re) spot-welded on the Mo ring under the sample. For a more accurate measurement, several infrared pyrometers with different temperature ranges are available.


*Figure 12. Elmitec sample holder with the cap mounted is shown on the left. Caps with different sizes of openings are shown in the center. The magnetic sample holder is shown on the right.*

There are several variants of sample holders available for different purposes. To achieve better performance at low temperatures with liquid nitrogen cooling, a copper-built sample holder can be used. For studying magnetic domains under a magnetic field, a sample holder with a built-in electromagnet can provide a bipolar out-of-plane magnetic field of up to 72 mT. Additionally, the sample holder can be modified to allow for the application of a current or voltage signal, either in a pulse or static manner, which is particularly useful for studying spin-orbit torque effect, ferroelectricity, and piezoelectricity.

In the preparation chamber, an Omicron flag-type sample plate can be transferred using an Omicron-Elmitec adaptor via a Ferrovac ultrahigh vacuum (UHV) 'suitcase' between the microscope and other external UHV systems, such as a scanning tunneling microscope (STM) facility. The transfer setup is depicted in Figure 13.

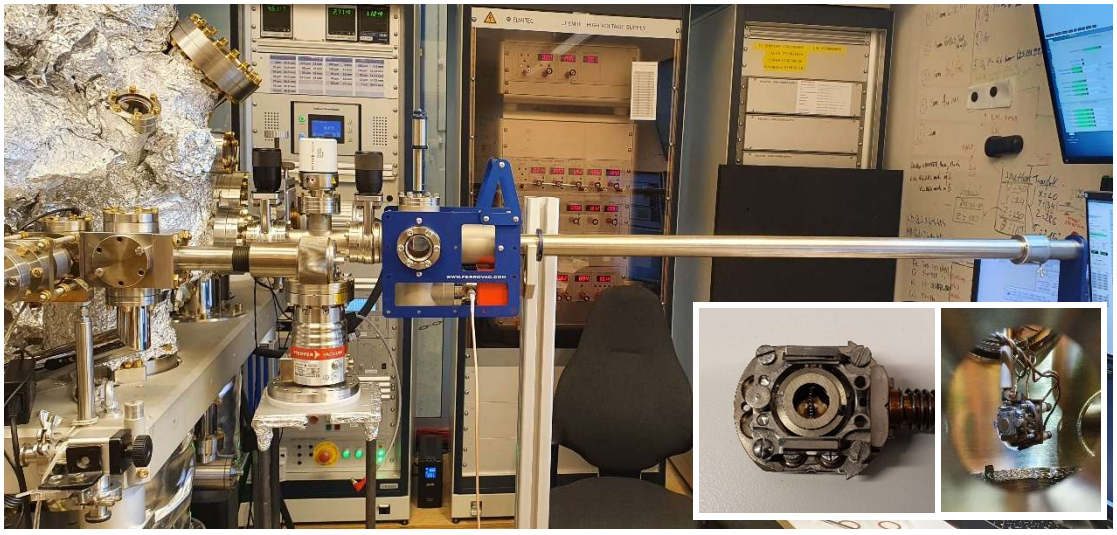

*Figure 13. A vacuum suitcase transfer setup, installed for a user beamtime. The insets show the Omicron-Elmitec adaptor sitting on the table and mounted onto the manipulator of the preparation chamber.*

### 2.2.5 Detector

Nowadays, most PEEM/LEEM systems use the MCP-CCD system to convert the final image from electrons into a grayscale image that can be shown and stored on a PC. However, the resolution of such a detector system is limited to about 130 µm, which corresponds to about 300 effective pixels across the 40 mm diameter of the MCP [11,12]. The dominant mechanism of image degradation is the lateral spread of the secondary electrons in the phosphor screen. With the new generation of ACSPELEEM microscopes, the old MCP-CCD detector will limit the overall system performance. To overcome this problem, a camera system that combines the traditional scintillator and the latest CMOS chip, from TVIPS Gmbh, was adopted in our AC-SPELEEM. In such a system, the 20 keV electrons first generate fluorescent photons on the scintillator layer. These photons are then transferred through the optical-fiber coupling unit to the CMOS chip. The detector is not bakeable but is very compatible with UHV as only the scintillator layer and the optical fiber array are inside the UHV chamber. After installing the detector into a pre-baked chamber that has a base pressure of $7 \times 10^{-11}$ Torr, the chamber pressure decreases to a low 10 scale within one or two days. The detector used in our microscope (TVIPS F216 model) with 16 mm physical pixel size has demonstrated 4× higher spatial resolution as well as two magnitudes higher dynamic range than the traditional MCP-CCD system. These improvements are shown in Figure 14.

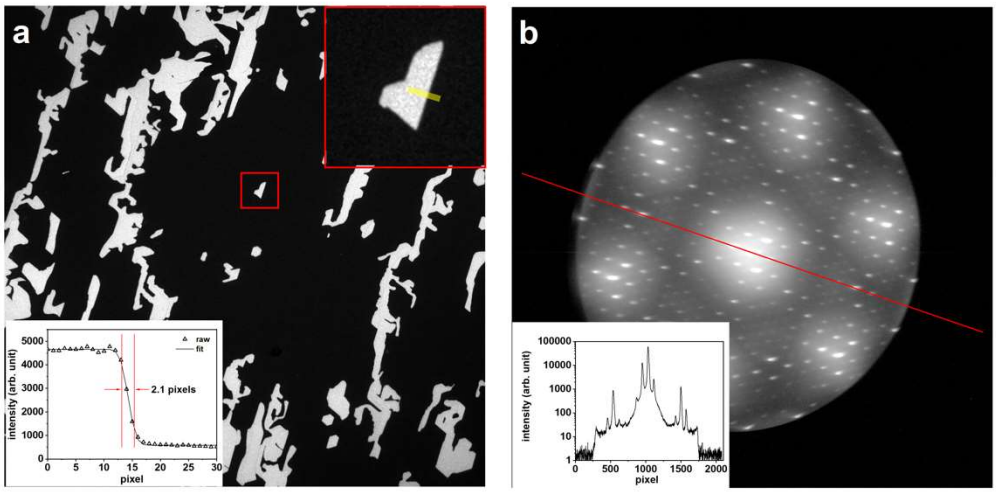


*Figure 14. (a) LEEM and (b) micro-spot LEED images from an epitaxial mono-/ bi-layer graphene sample grown on SiC to show the resolution and dynamic range of TVIPS-F216. The image size of (a) is 20 mm × 20 mm. The upper inset in (a) is the magnified image of the area selected in red (1484 nm × 1484 nm) and the profile across the mono-/bi-layer boundary (yellow line) is shown in the lower inset of (a). The resolution of the detector is determined to be about 2.1 pixels, which corresponds to 32.8 nm. The inset in (b) shows the profile along the red line across the LEED spots [note that the y-axis of panel (b) is specified on a logarithmic scale].*

### 2.2.6 Sample preparation and characterization

Sample preparation primarily occurs in the preparation chamber, where processes such as heating, sputtering, gas dosing, and material deposition can be performed. As demonstrated, the standard Elmitec sample holder features an integrated filament and thermocouple. The filament is insulated from the sample holder body, enabling the sample to be heated to over 2000°C for a brief period using E-beam bombardment. This configuration allows for the cleaning of refractory metals like tungsten.

The sputter gun, provided by SPECS GmbH, can operate at low power with a bombardment voltage under 1 kV, as well as in high-power mode with voltages up to 3 kV. Gas dosing, including the Ar supply for the SPECS sputter gun, is achieved through several pre-filled mini gas cylinders. These compact, palm-sized cylinders can typically be used for a year with moderate usage when filled with gas up to 4 bar in their 25 ml volume. Multiple CF 40 ports are available in the preparation chamber for users to install their evaporators or other UHV-compatible equipment. Crystal cleavage or exfoliation of 2D materials can also be performed in the preparation chamber using a wobble stick and transfer arm. Residual gas analysis is conducted using an RGA mass spectrometer from MKS, and a conventional LEED system from SPECS is installed for quick surface characterization.

Recently, with funding from a Vinnova project and in collaboration with Swerim, a more sophisticated temperature measurement and control system was implemented (Figure 15). This system, comprising pyrometers, PID control, and a Tango interface, has proven to be more accurate and reliable than the previous manual control system.

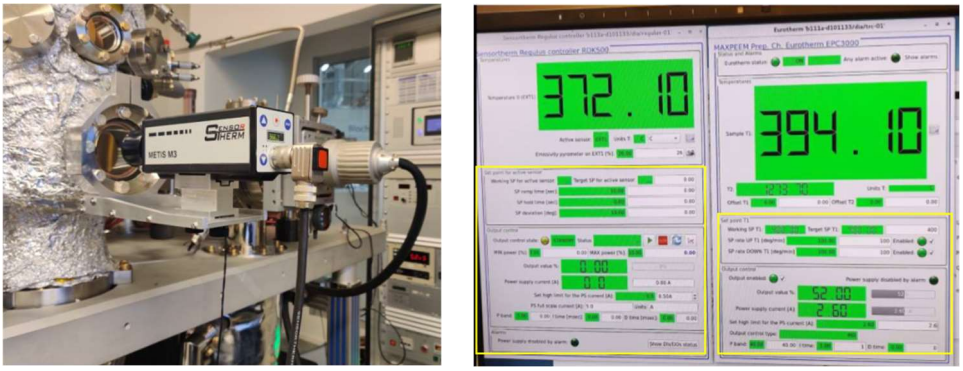


*Figure 15. A pyrometer is mounted onto the preparation chamber and measures the temperature of a sample independently of the built-in thermocouple. The project, called DEVPEEM, is supported by Vinnova.*

In the preparation hutch beside the experimental hutch, an optical microscope is mounted on a dedicated optical table and a highly stable micro-manipulator system with W probe tips is installed close to the microscope body, as shown in Figure 16. The inspection of a sample surface under the optical microscope is recommended to ensure the tidiness of the surface before loading the sample in the UHV chamber: the presence of micrometer-sized contaminants will most likely produce sparks during experiments in the SPELEEM microscope. The micro-manipulator allows both the removal of contaminants from the sample surface and the fine manipulation of nanostructures over the surface when needed.

### *2.2.7* Infrastructure

*The beamline consists of four hutches: the optical hutch, the control hutch, the experimental hutch, and the preparation hutch, shown in*

Figure 17. The optical hutch contains the primary optical elements of the beamline, including M1, the monochromator (grating and M2), M3, and the baffles for these mirrors. The final refocusing mirror, M4, is located inside the experimental hutch alongside the endstation. Intermediate elements, such as the exit slit and gas cell, are situated in the open space of the D building hall.

The experimental hutch features a dedicated ventilation and temperature control system, which can maintain temperature stability as precise as +/- 0.1°C. Currently, the control hutch serves as a temporary office for users. However, once full motorization of the microscope control becomes possible, operators will be able to remotely control the microscope from this room without affecting the temperature in the microscope hutch.

The preparation hutch houses the optical microscope with the micro-manipulator mentioned in section 2.2.6. This hutch also offers ample storage space for samples, vacuum parts, equipment, and tools.

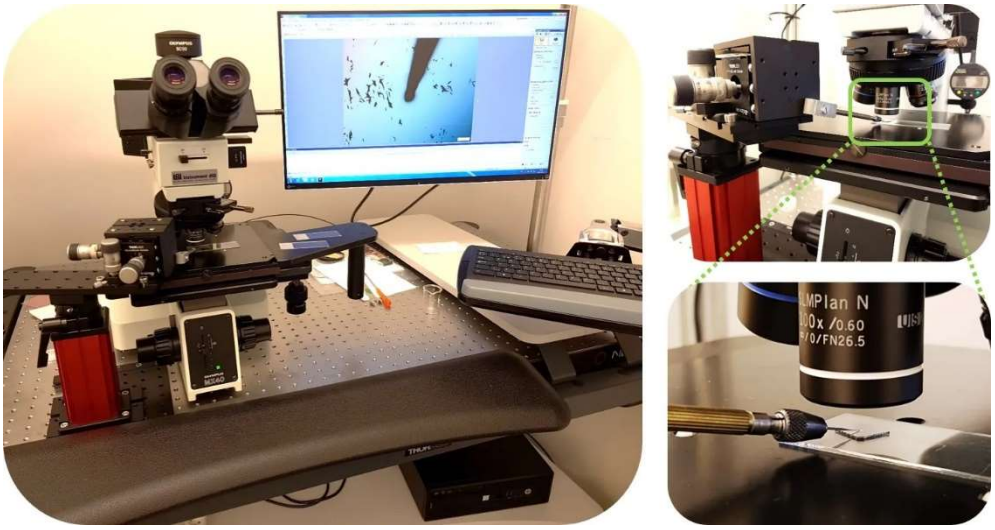


*Figure 16. The optical microscope located in the sample prep lab, equipped with a micro-tip manipulator.*

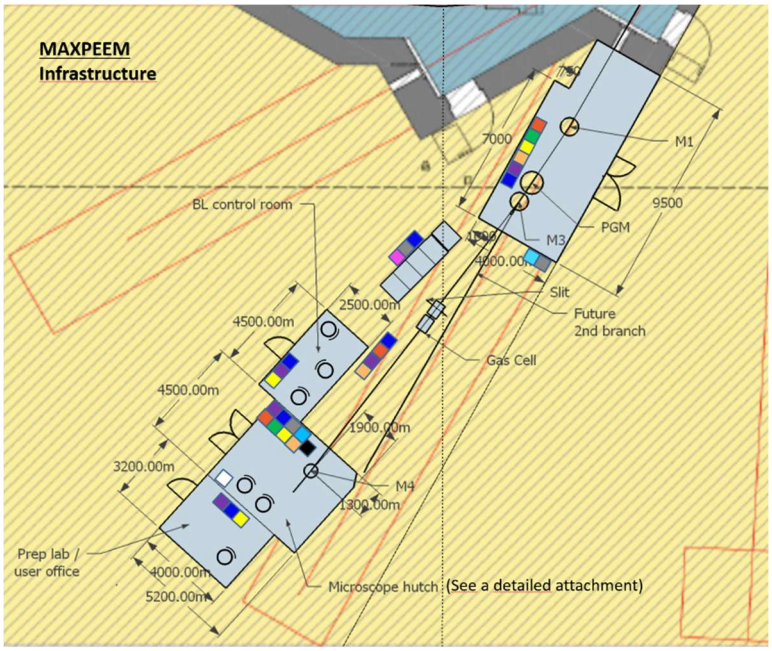


*Figure 17. The layout of the MAXPEEM beamline, showing the optics hutch, beamline control room, microscope hutch and prep lab.*

## 2.3 Competitive analysis

PEEM beamlines are found at nearly every synchrotron light source. These differ in a variety of aspects: pure PEEM versus LEEM/PEEM instruments, incidence angle of the synchrotron beam, and whether the instrument is equipped with an aberration corrector. Table 5 summarizes some performance metrics for MAXPEEM and several peer beamlines. Important beam parameters for PEEM beamlines are flux, spot size, resolving power, and energy range. MAXPEEM has the highest flux and the smallest spot size among beamlines with aberration-corrected instruments, while the resolving power and energy range are similar. In terms of publications, MAXPEEM is comparable to or slightly better than similar beamlines, with approximately 10 publications per year.

| | MAXPEEM (MAXIV) | UE56-1_SGM (BESSY) | UE49-PGM (BESSY) | 21-ID-2 (NSLS II) | BL24 – CIRCE (ALBA) | Nano-spectroscopy (Elettra) | I06 (Diamond) | Hermes (Soleil) | SIM (PSI) |
|---|---|---|---|---|---|---|---|---|---|
| Operation started | 2019 | 2012 | 201* | 2018 | 2012 | 2002 | 2007 | 2015 | 2001 |
| Number of publications | 41 | 23 | 126 (from 2009) | 27 | 117* | 248 (nanospec only, from 2002) | 208 (from 2007) | 145 (from 2008) | 200 (from 2012) |
| Energy range (eV) | 30-1000 | 55-1500 | 100-1800 | 20-1500 | 100-2000 | 25-1000 | 80-2100 | 70-2500 | 90-2000 |
| Aberration corrected? | Yes | Yes | No | Yes | No | No | No | No | No |
| Min. spot size [$\mu m^2$] | 15 x 15 | 40 x 40 | 20 x 10 | 50 x 50 | 12 x 36 | 20 x 3 | 10 x 3 | 25 x 7 | 100 x 30 |
| 2nd Branch | x | | | ARPES | APXPS | NanoESCA | Open port | STXM | |

*Includes the separate APXPS branch

*Table 5. Summary of performance metrics for MAXPEEM and several peer beamlines.*

# 3 Beamline operation

## 3.1 Modes of operation and key statistics

MAXPEEM received its first commissioning users in Spring 2019 and has been open for its first regular user proposals since Fall 2019, with a gradually increasing user load. Users can access MAXPEEM using the following type of proposals:

**Standard access** Beamtimes at MAXPEEM are allocated in aggregates of 4h-shift blocks, 24hr per day, during which the MAXPEEM staff guarantees 12hr of assisted operation. Mondays are reserved for accelerator needs, and Tuesdays were dedicated to beamline and insertion device commissioning until the fall semester of 2023, leading to 30 shifts per week for user operation. As of the spring semester of 2023, Tuesdays are given to users, thus a full week of beamtime is 36 shifts.

**Fast access** Apart from "normal" proposals, we offer an opportunity to apply for the fast access (FA). The FA proposals are foreseen for testing the sample or approach feasibility; or for time-critical experiments (breakthrough publication, PhD-thesis). Mainly, they should help (new) users in preparation of the normal proposals for a later call. The FA at MAXPEEM is at maximum 6 shifts (24 hours = 12 hr with operator) of beamtime per proposal. Due to the COVID-19 pandemic the beamline also developed a rudimentary **remote access** mode with no external users present.

**Industrial users** Proprietary access is open for industry, institutes, and private and public organizations providing commissioned research funded by industry. The access is covered by a non-disclosure agreement and the results belong to the users with no obligations for publication.

**Training & education access** Supporting the education of the next generation of scientists, MAX IV offers this special collaborative educational access mode for courses, training workshops or other similar activities. Historically, this used to be initiated by outside parties, e.g. as part of a university course or PhD workshop and negotiated on a case-by-case basis, followed by a formal application. Since the start of 2023 the application format is under review and it is at the discretion of the beamlines to schedule this kind of access. As the SPELEEM is also equipped with an electron gun and Hg lamp, educational activities can also be planned during offline days (eg. Mondays). MAXPEEM has participated in 1 (offline) educational day so far.

### *3.1.1* Proposal statistics

In the following graphs we summarize proposal statistics since the first open call in 2019. There are two cycles per year for access at MAXPEEM during the fall (**HT** - Höstterminen) or spring (**VT** – Vårterminen) semester.

Figure 18 gives an overview of the statistics for all standard access submitted proposals MAXPEEM received the past years, 75 in total. MAXPEEM maintains an average oversubscription ratio of 1.53, which is very good considering that shift allocation per proposal varies (Figure 19). A full week of beamtime at MAXPEEM comprised of 30 shifts. Since HT23, a full week has 36 shifts, and this also applied for selected weeks of VT23. As you can see in Figure 19, the average shift allocated per proposal is 21.4 shifts. The distribution and variety of demands per semester allows for the allocation of more than one proposal per calendar week.

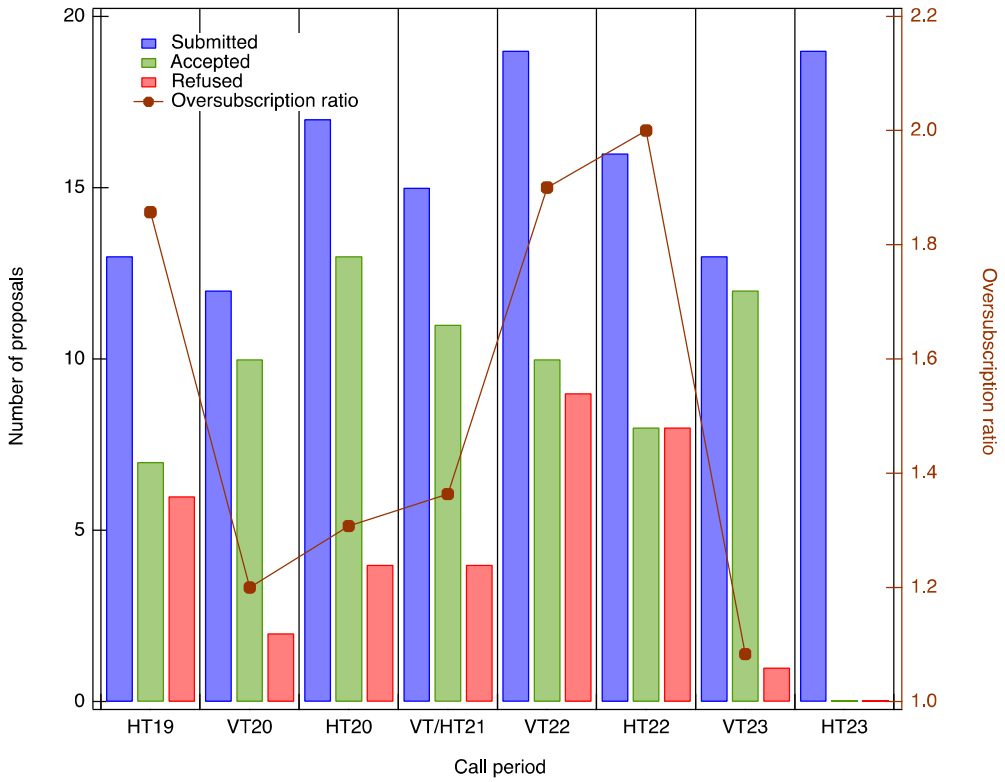


*Figure 18. Summary of submitted, accepted and refused proposals per call. The brown line represents the oversubscription ratio (Submitted/Approved); the y-axis is plotted on the right-hand side of the plot.*

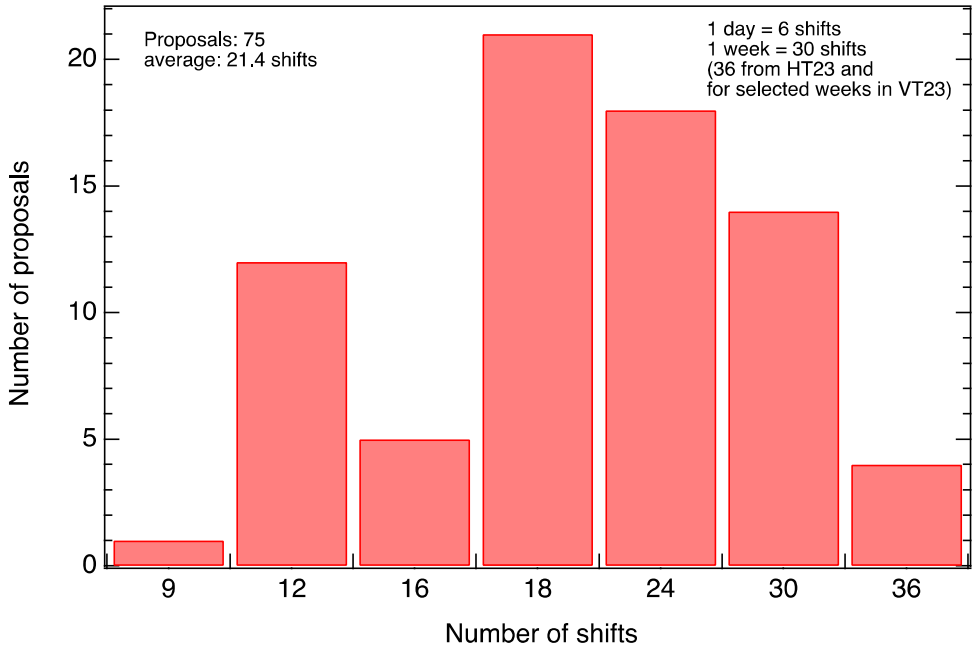


*Figure 19. Distribution of the number of assigned shifts for accepted proposals.*

In Figure 20, we present the distribution of proposals per research area. We tallied the proposals in five categories: surface science; 2D materials; materials; magnetism and industrial. More specifically, surface science includes studies that one could categorise as nanostructures, heterostructures, interfaces, thin films and flakes of more than one monolayer. 2D materials comprises of materials such as graphene, TMDCs or any other atomically thick layer. Materials contain studies of bulk matter that can be investigated with surface science methods (LEED, XPS, ARPES, XAS). Magnetism contains all studies where the focus is on magnetic materials and measurements mainly use XAS. Finally industrial, contains experiments focused on applications, for example steel and corrosion research.

The algorithm to categorise the proposals was the following (first affirmative answer gets the proposal):

1. (Magnetism) Do we used x-ray magnetic dichroism as a contrast mechanism for the proposal?
2. (2D materials) Is the material 2D?
3. (Surface science) Do we have an interface of 2D materials or thin film/nanostructures/flakes?
4. (Industrial) Do we have a direct connection of the material under study to industrial applications?
5. (Materials) The rest are binned here.

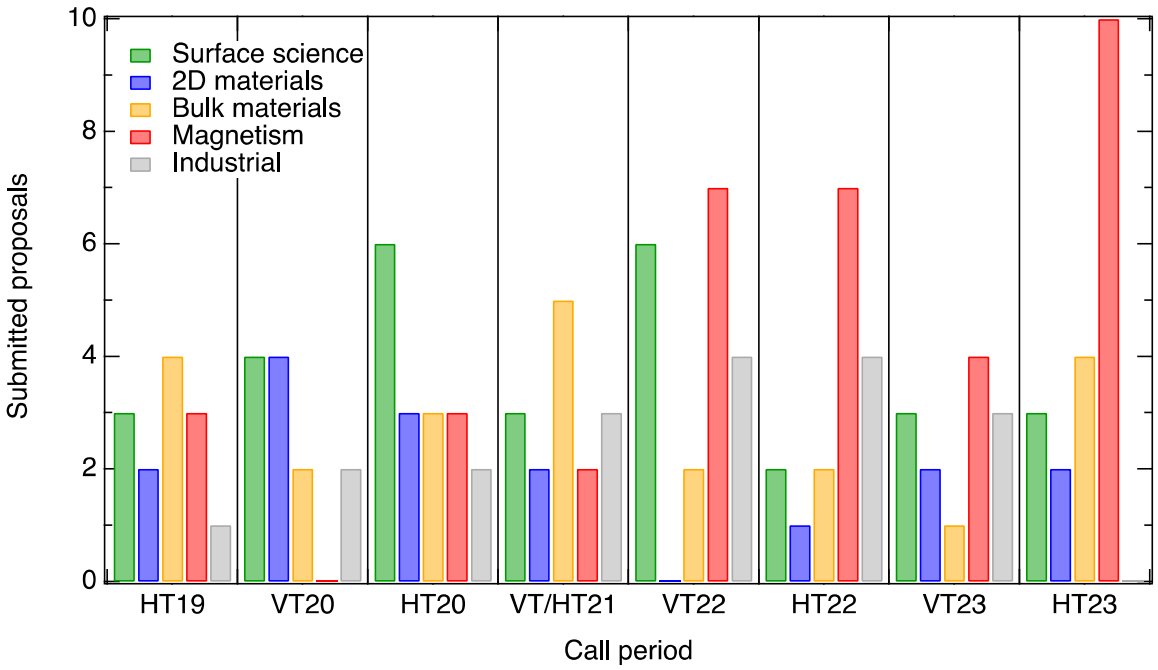


*Figure 20. Submitted proposals from recent call periods, grouped by research areas.*

A big chunk of our users comes from Swedish universities/research centres and over the years we accepted a lot of users from Europe (including the rest of the Nordics and UK) as well as users from USA, China, Australia and Brazil. Lately, see in Figure 21 where the data are summarised, an increased number of European users apply, and this can be linked to the increasing number of proposals in magnetic materials (Swedish magnetic community is active but small).

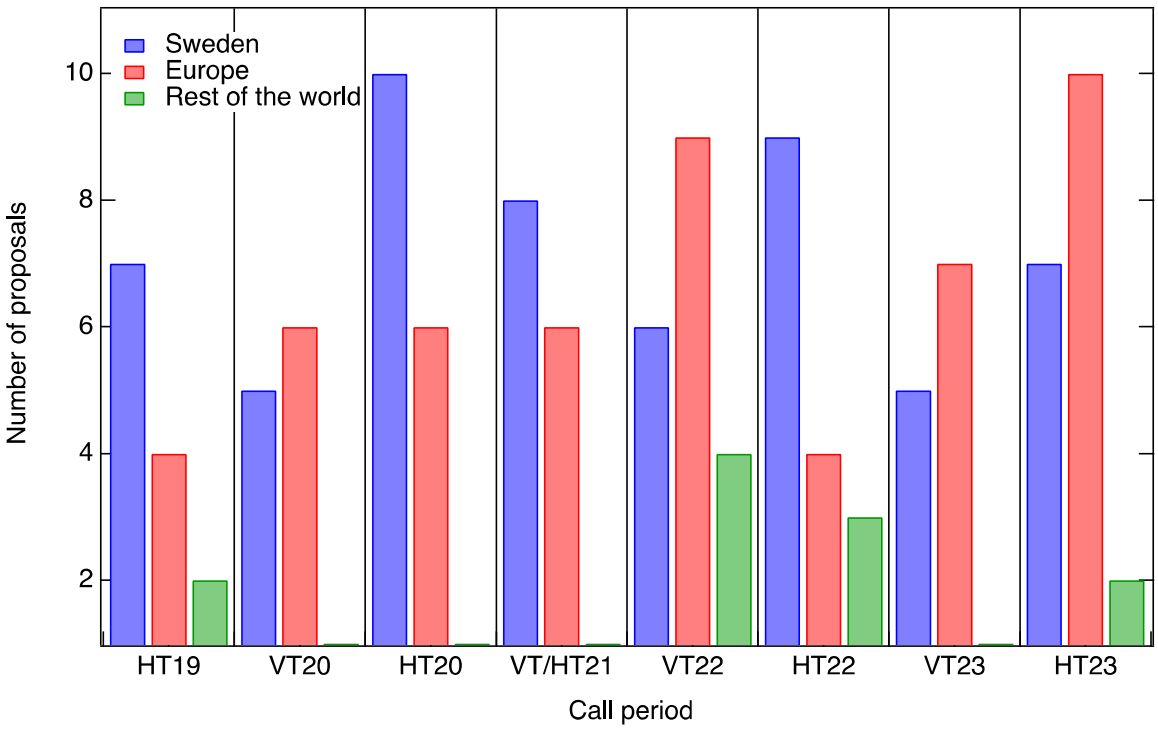


*Figure 21. Region of origin of MAXPEEM users. Proposals are assigned to a region based on the affiliation of the main proposer.*

### *3.1.2* User feedback

The user feedback summarized here is current as of March 2023. Year in the plot below (Figure 22) and table in the Appendix specifies when the experiment was performed, not when the feedback was submitted. Due to insufficient statistics for years 2018 and 2023, they are not summarized in the plot below.

Several trends emerge from Figure 22. One, scientific support by the beamline staff consistently earns the highest fraction of 5/5 grades. Second, the fraction of users who rate their beamtime as a 5/5 remains steady over time – despite fluctuations in the other parameters. Third, the fraction of users complaining about IT services (data transfer, Wi-Fi, etc.) has steadily decreased over time. Fourth, improvements to beamline documentation and software could be made. The data for Figure 22 are presented in the Appendix.

### *3.1.3* Publications

The following statistics in Table 6, current as of April 13, 2023, apply to work performed at MAXPEEM and not I311-PEEM. We note that papers arising from work performed at I311-PEEM are still being published.

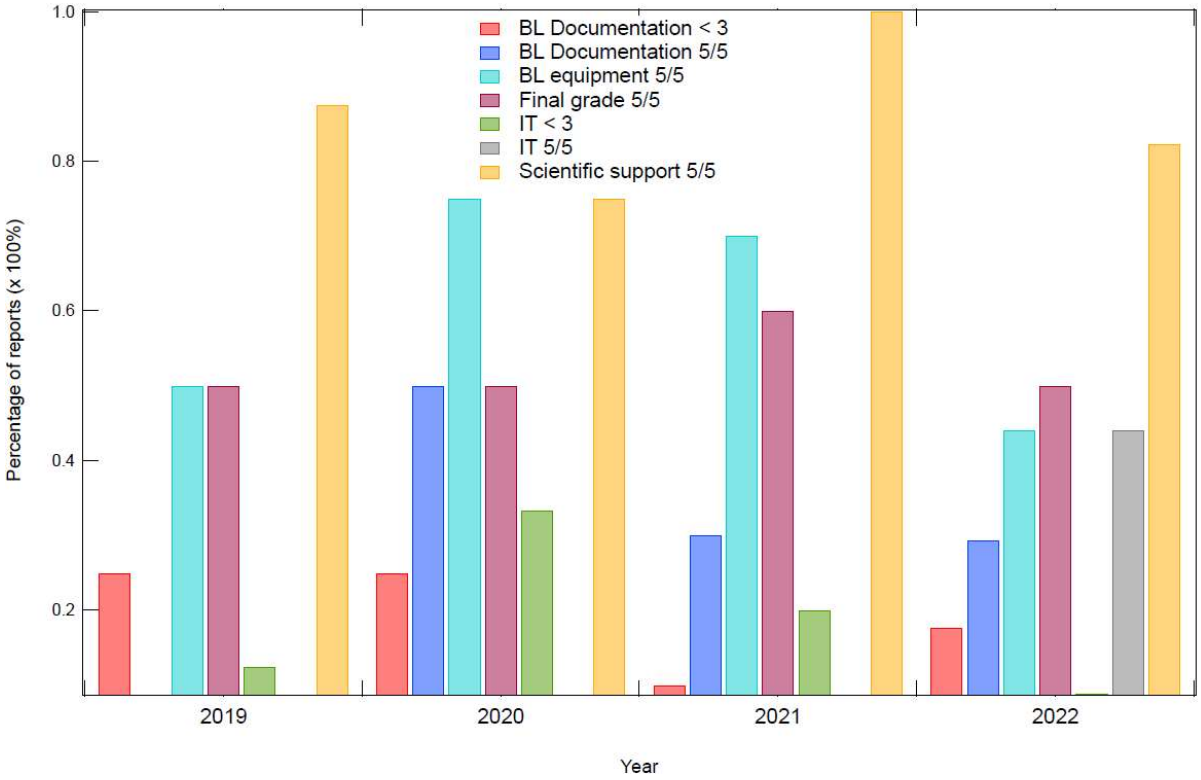


*Figure 22. Summary of key grades from user feedback. The y-axis shows a percentage scale.*

| Year | Number of publications | Number, high-impact publications (JIF > 7) | Topical areas |
|---|---|---|---|
| 2023 | 6 | 4 | 2D materials, heterostructures, beamline paper, photocatalysis, optoelectronics, antiferromagnetic spintronics |
| 2022 | 9 | 3 | 2D materials, carrier dynamics, stainless steel alloy, ferroelectrics, heterostructures, (photo)catalysis, nanomaterials, batteries, graphene |
| 2021 | 11 | 6 | Antiferromagnetism, graphene, catalysis, semiconductor doping, heterostructures, steel, nanomaterials, |
| 2020 | 9 | 5 | graphene, gas sensing, heterostructures, 2D materials, doping, epilayers |
| 2019 | 6 | 2 | Nanoelectronics, graphene, aluminum oxide, operando, metal oxidation, electronic correlation |
| 2018 | 7 | 5 | Steel alloying, graphene, photocatalysis, nanomaterials, quantum charge transport, metal-insulator-transition, metal oxides, electrical contacts |
| 2017 | 2 | 1 | Pristine/intercalated graphene |
| **Total** | 50 | 26 | --- |

*Table 6 Publication statistics*

## 3.2 Staffing

All beamlines were originally planned with a staffing of 4 positions: two permanent beamline scientists (BLS), one permanent instrument scientist (IS) and a postdoc (2 year, with refill), where one of the BLS is usually taking the role of beamline manager (BLM). The BLM position carries tasks like beamtime scheduling, as well as budget responsibility, and a general steering of the course of the beamline concerning developments and upgrades, of course aided by the rest of the team. The distinction in the educational background & experience of a BLS and IS at MAX IV has often been proven to be negligible, and as such, MAXPEEM is now a beamline with 3 BLS and a postdoc. Supplementary to this, additional staff (postdocs, visiting scientists) can be added with the help of outside financing, and MAXPEEM has had both in the past, as a result of scientific grants (Zakharov) and a Chinese exchange program.

The current MAXPEEM team members are:

**Alexei Zakharov**: BLS at MAX IV since 2001, who secured the grant for the initial purchase (and subsequent upgrades) of the SPELEEM instrument. BLM for MAXPEEM since its conception in 2013. Participates in user support and local contact duties.

**Yuran Niu**: BLS, permanently employed at MAX IV since 2018, and previously (2012-2016) as postdoc & temporary researcher. Participates in user support and local contact duties.

**Evangelos Golias**: BLS, permanently employed at MAX IV since 2021, previously at BESSY II synchrotron and FU Berlin. Participates in user support and local contact duties.

**Gabriel Man**: Postdoc, employed since Nov 2022 on a 3 year contract. Participates in user support and secondary local contact duties. Starting up an in-house research program on perovskites.

The MAXPEEM beamline is part of the Imaging group, which also comprises NanoMAX (hard x-ray nanoprobe), SoftiMAX (soft x-ray scanning & coherent imaging) – both on the 3 GeV ring – and the SPM-lab: a support lab with STM, AFM and SEM/EDX instruments.

## 3.3 Typical beamtime process: from allocation to support

**Beamtime allocation**

Proposal rounds at MAX IV occur twice per year, and the allocation of available beamtime follows a protocol that is uniform across the facility. After the beamline team performs a basic technical feasibility check, all proposals are sent for scientific review to the program advisory committee (PAC), along with comments, when needed, re technical issues of each proposal. The beamline team does not comment on the scientific value of the proposals so that PAC can evaluate the proposals unbiased. Any safety concerns are also flagged by the beamline staff here, or after the PAC meeting, during a Safety run through of the accepted/reserve list proposals with the Experimental Safety Team.

**Beamtime scheduling**

Accepted proposals are scheduled at the beamline. The beamline manager takes the responsibility of the allocation of beamtime to the users, trying as much as possible to respect users' wishes/constrains. The beamline manager assigns a local contact (LC) for every allocated beamtime who takes care of further coordination. LCs are allocated based on history with a particular group, specific interest towards the proposal's topic and availability during the scheduled calendar week. At MAXPEEM, along with the LC, the role of the helper is internally distributed. The helper is a second person that supports the experiments during beamtime.

**Preparation for beamtime**

LC checks and confirms all experimental details described in the proposal, establishing whether any special preparations need to be made at the beamline or by the experimental group ahead of time. The LC ensures that all equipment needed for the experiment is in place and in good working order. Finally, the LC guide the users through MAX IV administrative and safety requirements.

**Support during beamtime**

At MAXPEEM, during beamtime the LC and helper are present in shifts and they are responsible for the operation of the microscope and data acquisition for the morning, afternoon, and early evening shifts (LC/helper work shifts 8-16/12-20). Support outside of these hours is sometimes possible (shift 8-16/14-22) but generally considered as overtime. **Most of the experiments do not run overnight when the beamline personnel cannot be present.** There are exceptions where the users can run the experiment during the day or night, for example, in magnetic studies when only the beamline parameters need to change and not critical parameters of the microscope.

**Facility support**

There is also on-call support available at the facility level to both users and to beamline staff during non-office hours, from all major divisions in the laboratory (e.g. IT & experimental & radiation safety: until 23:00, and accelerator, PLC, water & electrical 24/7). In addition to this a program of staffing 24/7 on-site 'floor coordinators' has recently begun, aiming to provide a constant, centralized point of contact for both users and staff for emergencies on the one hand, or mundane tasks (eg. locating gas bottles, filling liquid nitrogen dewars, etc) on the other hand.

## 3.4 Community outreach

Naturally, MAXPEEM has inherited many users from Beamline I311 of the old Max-lab. In addition to this, we have expanded our user community through the following channels:

**MAXPEEM webpages:** The beamline webpages provide all relevant information on capabilities, equipment status, and data analysis programs that potential and current users may need.

**Fast Access mode of operation:** MAXPEEM is among the first few beamlines to offer this mode to the user community. With one or half-day beamtime, many users can perform feasibility checks on measurements, potentially attracting them as regular users.

**Users' publications and conference presentations:** User publications and conference presentations showcasing work done at the beamline, as well as word-of-mouth in the research community.

**Dedicated talks about MAXPEEM:** We have delivered such talks in seminars organized by the user office of MAX IV for researchers and PhD students from various Swedish universities, such as the Royal Institute of Technology (KTH) and Luleå University. Beamline staff also attend other workshops and conferences to introduce MAXPEEM to the audience.

**Other channels provided by MAX IV Laboratory:** These include internal seminars such as MAX IV Scientifika and Science and R&D seminar series, the MAX IV user meeting featuring beamline presentations and posters, and scientific subsections, as well as targeted newsletters for specific categories of users and other interested parties about the beamline's status and progress.

**Beamline paper:** A paper detailing beamline specifications, measurement capabilities, and instrumentation studies was published online on February 3, 2023, by the Journal of Synchrotron Radiation.

**Direct collaborations with other research groups:** All staff at MAXPEEM have research interests in different fields. By collaborating with people who share common interests, the MAXPEEM team brings them to conduct experiments at MAXPEEM.

# 4 In-house research

## 4.1 Ambivalent behaviour of germanium-intercalated graphene: interfacial dynamics

The functionalization of graphene is essential for realizing graphene-based electronic and photonic devices; tuning the chemical potential by doping via intercalation is one of the most promising approaches. The intercalation of germanium is particularly interesting due to its ambivalent doping behaviour. Both p- and n-type graphene and their doping levels were identified with XPEEM and LEEM (Figure 23) and ARPES (Figure 24) [13].

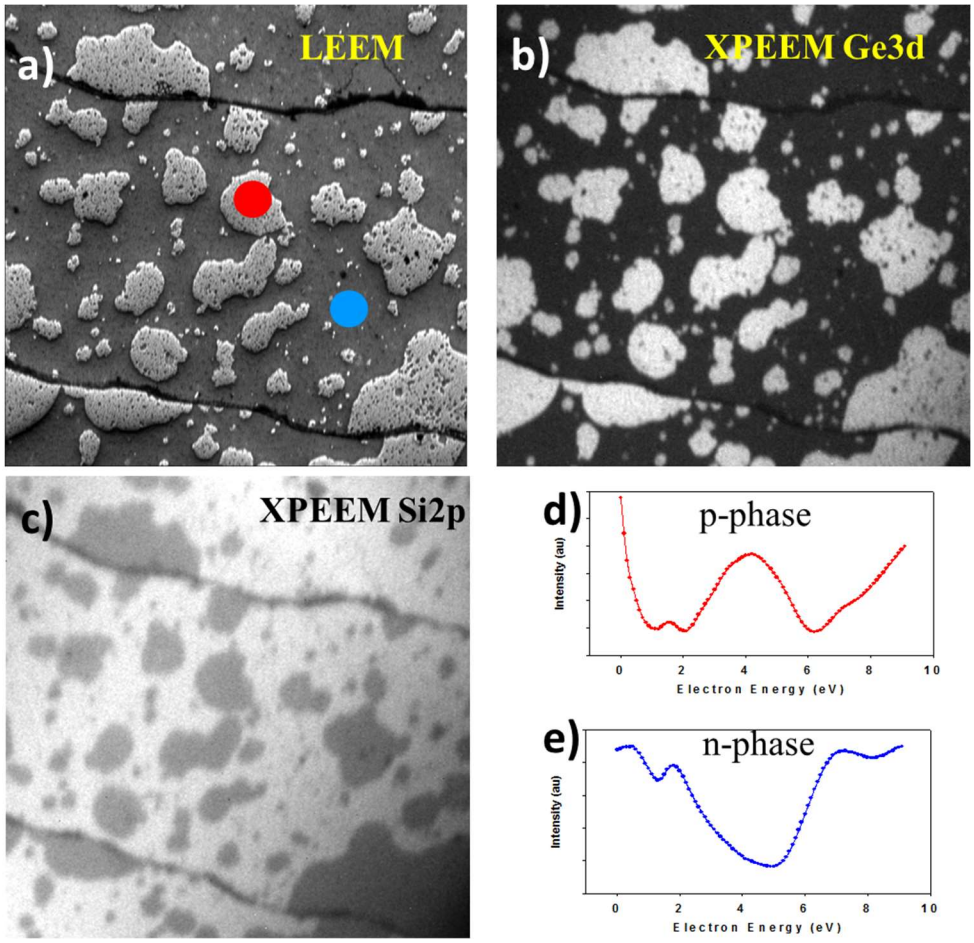


*Figure 23. Real space characterization of the mixed phase in Ge-intercalated graphene. a) LEEM image (electron energy 3.5eV) showing the islands of p-doped phase in the sea of the n-doped phase. The height difference between p- and n-phase in the LEEM image is emphasized by moving the contrast aperture slightly away from the optimal position. b) Ge3d XPEEM image of the same area as in a). The white islands belong to the p-phase that has twice as much germanium compared to the n-phase. Photon energy hv=100eV, electron kinetic energy 64eV. c) Si2p XPEEM image showing an extra attenuation of the Si2p photoelectrons going through the p-type islands. Photon energy hv=150eV, electron kinetic energy 45.2eV. Field of view is 100 µm for all three images. d) and e) LEEM I-V curves collected from areas marked by red and blue circles respectively in the LEEM image (a) displaying a dramatic difference in the reflectivity of p- and n-doped Ge intercalated graphene.*

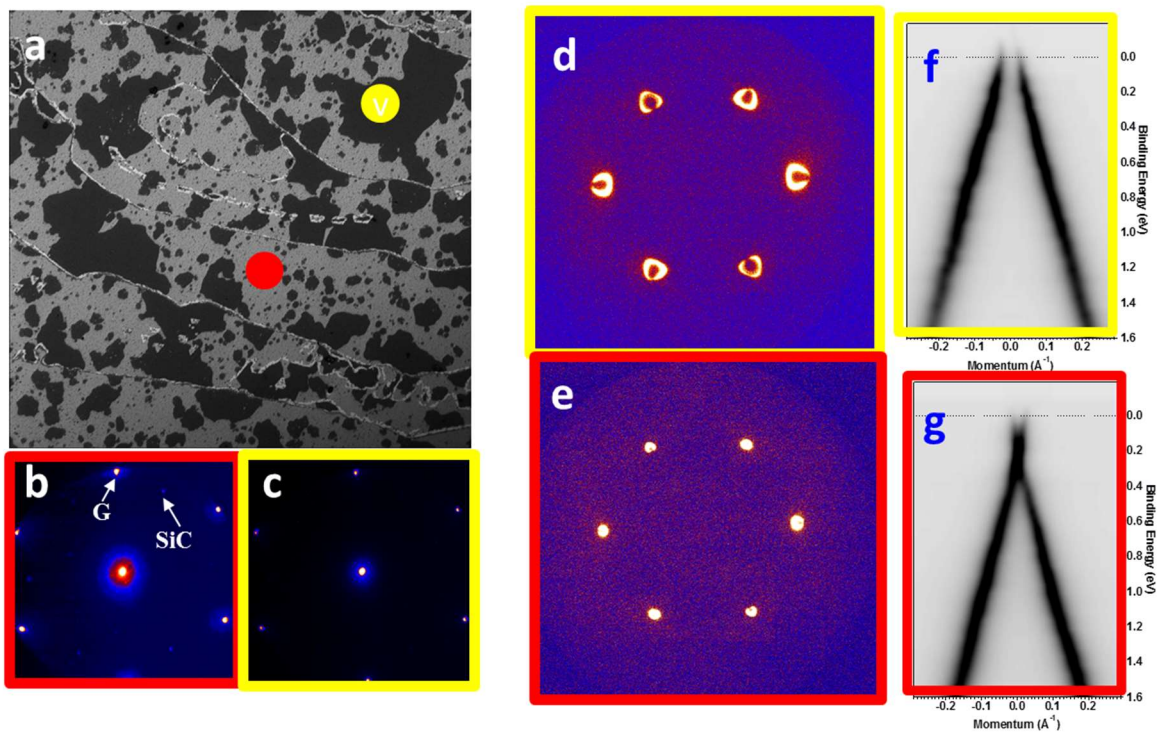


*Figure 24. Reciprocal space (diffraction) characterization of the Ge-intercalated graphene. a) LEEM image of the surface, recorded using an electron energy of 6.5eV, FoV=25 μm. Yellow and red circles depict the areas where all diffraction data were collected (sampling area 1.5 μm). b) and c) low energy (50eV) electron diffraction (LEED) from the n-doped and p-doped graphene, respectively. d) and e) ($K_x$,$K_y$) photoelectron diffraction pattern acquired at Eb=0.2eV below the Fermi level from p-doped and n-doped areas, correspondingly. Photon energy 45eV. f) and g) E(k) plot perpendicular to the G-K direction for the p-doped and n-doped phase, respectively.*

## 4.2 Rectangular 2D phosphorus lattice on Ir(111)

After nearly a decade since the rediscovery of black phosphorus (BP) and the realization of its great potential for logic applications, we are still in search of a breakthrough in BP epitaxial growth, which remains an open problem [14]. We recently synthesized on Ir(111) a two-dimensional phase of P with ***rectangular symmetry*** (the symmetry of a BP monolayer, i.e. phosphorene). Low-energy electron diffraction (LEED) and scanning-tunnelling spectroscopy (STM) revealed the formation of large domains with rectangular symmetry and a relative arrangement that is threefold symmetric – imposed by the hexagonal symmetry of the substrate (Figure 25(a)-(f)). ARPES experiments at BESSY-II synchrotron in Berlin (Figure 25(e,f)) revealed a rich electronic structure of the P overlayers. The study about the nature of this new P 2D structure is underway and future experiments at MAXPEEM along with DFT calculations will help us understand the link between the structure we created with black phosphorus.

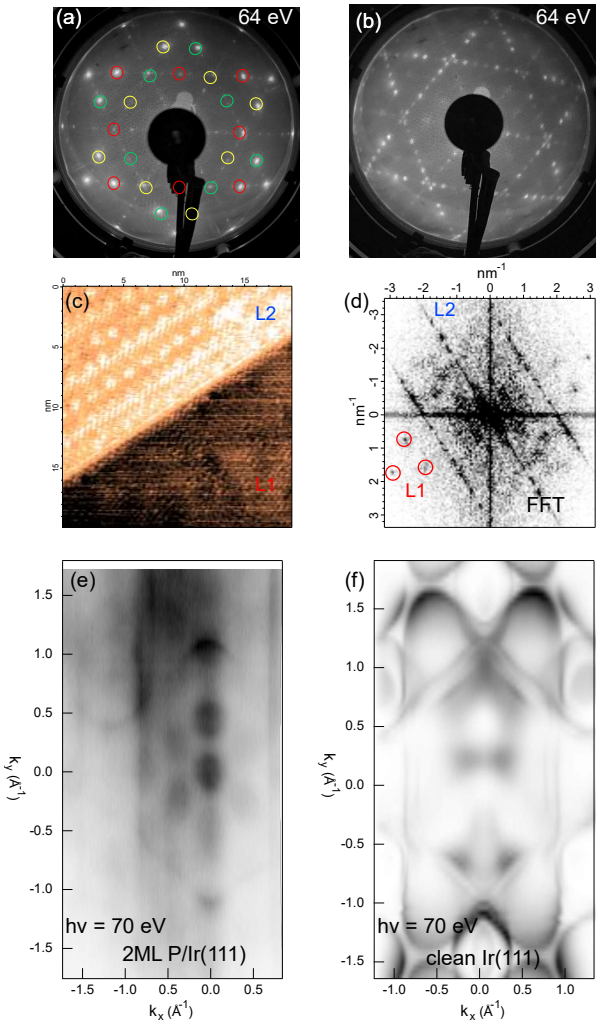


*Figure 25. LEED patterns of (a) 1ML P on Ir(111) and (b) 2ML P on Ir(111), using electrons with kinetic energy of 64 eV. Different colors mark the reciprocal lattice of the three equivalent domains. (c) STM image of a region with 1 ML (L1) and 2 ML (L2) P coverage. We can see the three different domain orientation at the bottom of the image. (d) FFT transform of (c). ARPES Fermi surface measurements of (e) 2ML P/Ir(111) and (f) clean Ir(111).*

## 4.3 Phosphorus chains on Ag(111)

Phosphorus exhibits allotropism, where the allotropes feature diverse crystalline structures and properties, and black and blue phosphorus are currently the most prominent members for surface science and electronics [15,16]. Recently, the creation of phosphorus nanoribbons with chemical methods has paved the way for engineering the electronic properties of low-dimensional phosphorus, in a similar manner to graphene nanoribbons [17]. Most recently, the first successful growth of one-dimensional phosphorus chains has been reported on Ag(111) [18]. The link between 1D phosphorus nanoribbons/chains on Ag(111) phosphorus is not clear and there are open questions about the connection between dimensionality and electronic structure of low dimensional phosphorus on Ag(111).

In early 2023, we studied the evolution of growth from 1D phosphorus chains to 2D phosphorus live using LEED at MAXPEEM. We identified (Figure 26) a new reconstruction of 1D chains (4x1, see S4 in Figure 26) before the onset of the 3x1 phase (S1) of 1P chains, the precursor of the 2D phosphorus phase.

This study is a follow-up investigation of our first results on P chains studied with our collaborators in the project from BESSY-II in Berlin. You can read about our first results on arXiv (manuscript currently under review at Nature Communications) [19].

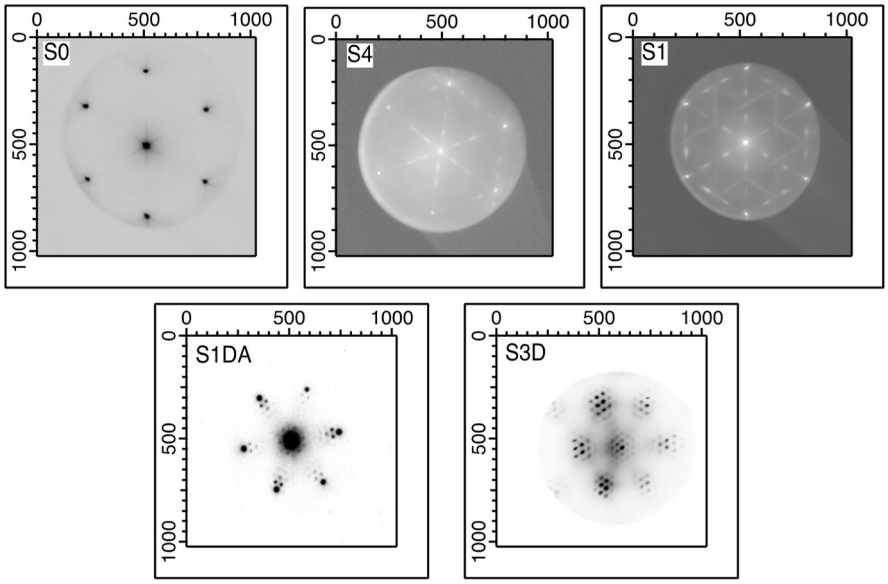


*Figure 26. LEED images of different samples. S0: clean Ag(111). (S4) 20 min P deposition at RT. (S1) 30 mins P deposition at RT. (S1DA) transformation to 2D chains after annealing S1 for 15 mins at 230°C. (S3D) 1hour P deposition on Ag(111) at 230°C.*

## 4.4 Growth mechanism of highly dipolar semiconducting molecules on SiC/graphene

Merocyanines are small-molecule organic semiconductors that are used for dyeing textiles, as fluorescent probes in the biomedical field, as light absorbers in organic solar cells and in numerous other applications [20]. Lab-scale, single-junction organic solar cell power conversion efficiencies are on the threshold of 20%, which is a threshold for technology development, and one of the key enablers is morphological control of donor and acceptor domains on the nanoscale [21,22]. Substrate-based templating is one approach for realizing bulk morphological control. A second motivation for understanding/controlling the growth of organic semiconductors is to design/tailor the substrate/organic interface. The energy level or band alignment at device interfaces is crucial for carrier extraction/injection and is critically dependent on molecular stacking/orientation.

In collaboration with the group of Dr. Selina Olthof (Institute of Physical Chemistry, Universität zu Köln), which performs home lab-based ultraviolet and inverse photoelectron spectroscopy (UPS, IPES), and their collaborators at the University of Bonn (Sokolowski group), which synthesizes the dipolar merocyanine molecule HB238 and performs STM, we will use LEEM, recorded live during deposition, to investigate the morphology of sub-monolayer, monolayer and multilayer growth of HB238 on SiC/graphene. The Olthof group has performed UPS measurements and obtained values for the work function and ionization energy as a function of expected film thickness (Figure 27(left)). By complementing these measurements with LEEM, we correlate morphology with variations in device-relevant electronic structure.

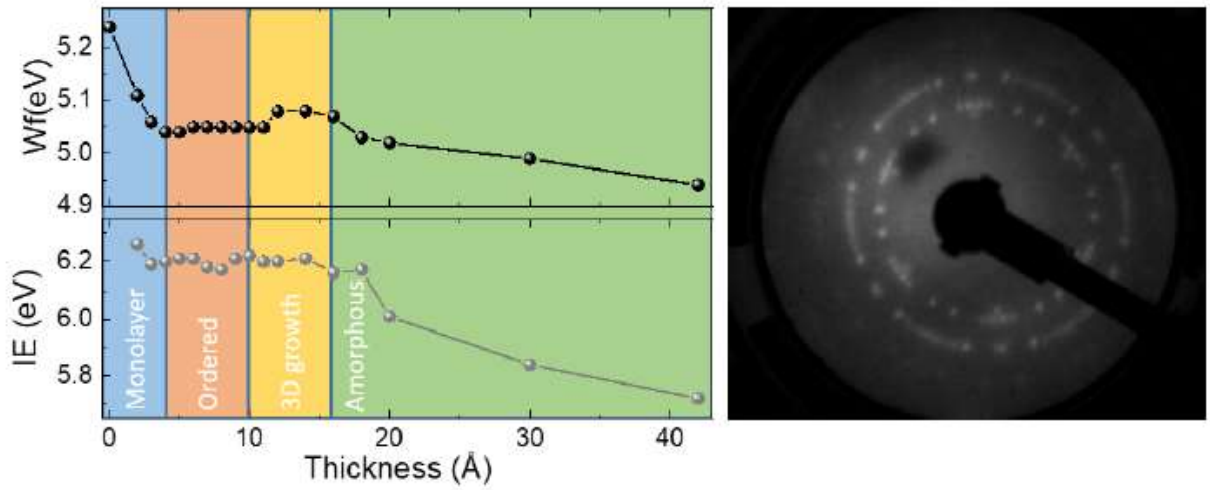


*Figure 27. Measured values of work function and ionization energy, obtained with ultraviolet PES, as a function of HB238 film thickness (left). LEED image of 4Å HB238, recorded with 26 eV electron energy (right).*

The current interpretation of the IE/WF as a function of film thickness trend, is that beyond a critical thickness of ~18Å, the film becomes amorphous. Figure 28 shows our current model of film growth. Growth of HB238 in the monolayer regime (~4Å) shows ordering (Figure 27(right)). As one of our objectives is to understand, then control, the growth of a highly dipolar molecule, this project offers an opportunity to investigate molecule-molecule versus molecule-substrate interactions in-depth, with potential impact on the design and deposition of organic semiconductor-based (opto)electronic devices. The expectation from the Bässler model is that organic compounds that lack dipole moments are considered optimal for charge transport, as the increased energetic disorder associate with dipole moments is thought to impede charge hopping [20]. We expect to validate, disprove, or extend this line of thought.

The chemical design space of organic semiconductors is vast, limited only by the ability of synthetic chemists to visualize and create the molecules, and LEEM has been successfully applied to the study of layer-by-layer growth of organic molecules on substrates [23]. We expect this project to stimulate increased interest from users in this research field in MAXPEEM.

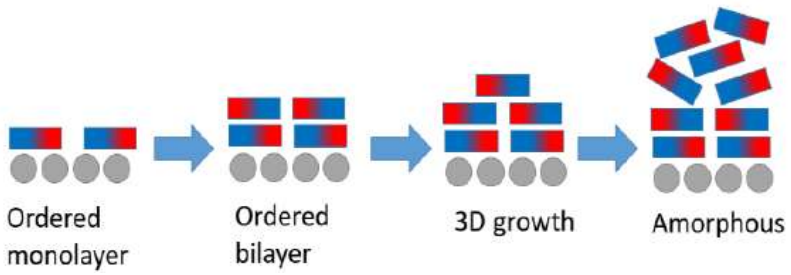


*Figure 28. Suggested growth mechanism of HB238 on SiC/graphene.*

## 4.5 Surface degradation mechanism of in-vacuum cleaved monocrystals of lead mixed iodide-bromide perovskites

The certified power conversion efficiency of lab-scale, monolithic silicon/perovskite tandem solar cells (33.2%) has now exceeded that of the best single-junction solar cells (e.g. perovskite-only (25.8%), silicon (26.8%), gallium arsenide (29.1%)), and global development of silicon/perovskite tandem technology is progressing rapidly (including in Sweden, at Evolar (now First Solar) in Uppsala). In addition to their expected low cost of fabrication (high optoelectronic quality semiconductors processed from solution) and various other features, halide perovskites feature bandgap tunability via simple halide mixing in solution. In contrast, multijunction cells that feature a stack such as GaInP/GaAs/Ge require expensive epitaxial growth techniques.

Given the ~1.1 eV bandgap of silicon, the optimal perovskite bandgap ranges between 1.7-1.8 eV in a tandem cell [24]. Pure iodide perovskites possess a bandgap of ~1.5 to 1.6 eV and pure bromide perovskites possess a bandgap of ~2.3 eV, hence to engineer an optimal silicon/perovskite tandem solar cell a mixed iodide-bromide perovskites with a ~1.7 to 1.8 eV bandgap is needed. Halide migration/segregation of mixed-halide perovskites, triggered by solar irradiation for example, has widely been observed, though the segregation and self-healing mechanisms and identification of key factors governing the terminal composition(s) are controversial [25]. This was particularly evident at a recent workshop held in Lund (May 10-11, 2023, organized by Ivan Scheblykin at Lund U and Eva Unger at HZB).

The migration of mobile ions and the resulting ion/vacancy accumulation/depletion at the interfaces between the perovskite and the contact/electrode layers of a device is expected to substantially impact the operational stability and band alignment; from a device standpoint, perovskites could be "all about the interfaces" [26]. Consequently, one of the prerequisites for developing viable > 20 year lifetime perovskite solar cell technology is to understand, and then subsequently manage the chemical-structural-electronic structure changes occurring at the device interfaces. Here we use the multi-modal capability of spectroscopic microscopy at MAXPEEM and the intrinsic surface sensitivity originating from measurements of electrons with low and relatively low kinetic energies to correlate chemical-crystal structure-topography-electronic structure changes at the surface, relevant for interfaces. This research thread overlaps fundamental, applied and industrial research and is timely and crucial for global societal sustainability. Halide migration/segregation will be induced under controlled irradiation conditions (X-rays only, X-rays + simulated solar irradiation). Expected experimental outcomes include the identification of (i) transient chemical species formed at the surface during illumination (using XPEEM, micro-XPS, XAS-PEEM), and potential observation of changes in the (ii) crystal structure (micro-LEED), (iii) surface topography (LEEM) and (iv) electronic structure (micro-ARPES). The chemical-structural-electronic correlation enables us to propose/validate/refute mechanisms with greater certainty. Once a basic understanding of the mechanism(s) has been obtained, we aim to introduce additives onto the surface (using a self-assembled monolayer (SAM) for example) to manage chemical/structural changes.

Several technical advances are needed for this work: (i) ultraclean model surfaces, (ii) flat surfaces, and (iii) beam damage management. First, we have previously succeeded with developing tools and a methodology for preparing ultraclean and model surfaces from in-vacuum cleaving of halide perovskite monocrystals, and are adapting the methods for use at MAXPEEM (as part of the endstation development) [27,28]. Second, flat surfaces are needed due to the requirements of the microscope; a high electric field of ~60 kV $cm^{-1}$ is present between the sample surface and microscope objective to

accelerate low energy electrons to higher kinetic energies so they can be efficiently steered inside the microscope. A rough surface will likely lead to capacitive breakdown in vacuum (arcing), damaging the sample, potentially contaminating the microscope objective, and preventing measurement. Our recent XPEEM measurements on glovebox-cleaved halide perovskite monocrystals showed that it is feasible to perform measurements (Figure 29). Third, halide perovskites are susceptible to photon/electron/etc. beam damage; we have previously succeeded with synchrotron-based measurements on this class of materials.

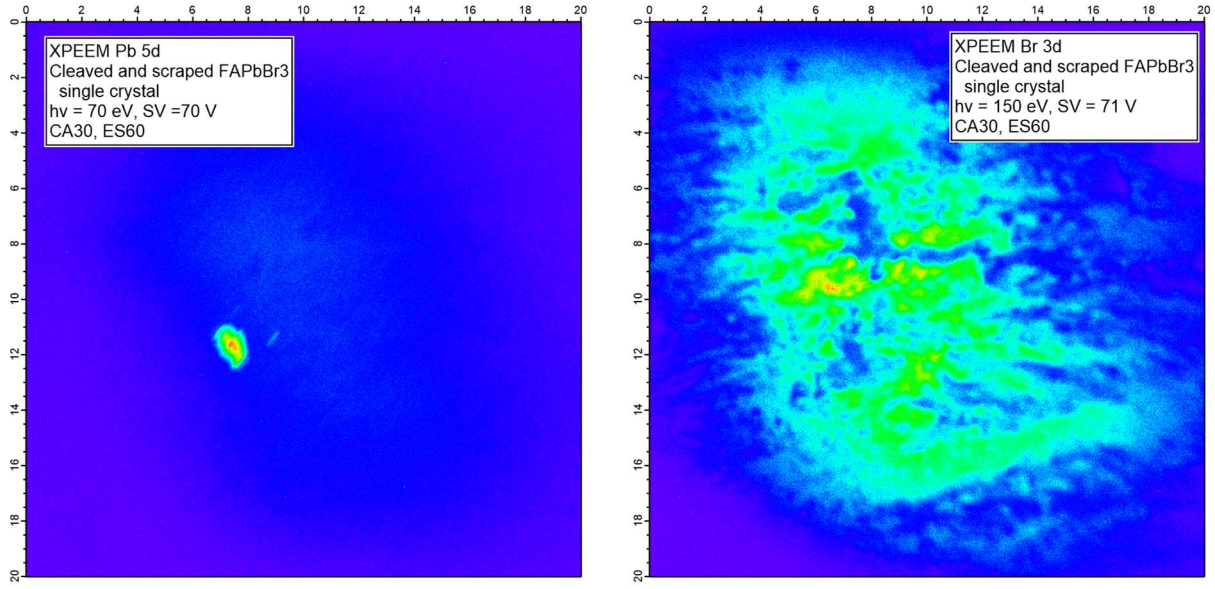


*Figure 29. First XPEEM images of a cleaved lead halide perovskite monocrystal obtained at MAXPEEM. (left) lead 5d XPEEM. (right) bromine 3d XPEEM. The monocrystal was cleaved ex-situ in a glovebox.*

The investigation of monocrystal surfaces with UHV-based PEEM/LEEM is the first step; perovskites utilized in devices are not exposed to vacuum during operation. The vacuum itself may exacerbate the diffusion of mobile defects/ions to the surface, then form volatile species that are pumped away. The next step is to utilize the same types of measurements in a more realistic environment, using for example near ambient-pressure PEEM/LEEM (NAP-PEEM/LEEM). Such instruments are starting to be deployed and a NAP-PEEM endstation is under consideration for the second branch of the MAXPEEM beamline [29].

## 4.6 Instrumentation: aberrations and space charge effects

Correction of main aberrations (spherical and chromatic) in the electron microscope is one of the most significant breakthroughs in improving the spatial resolution of the instrument. The spherical ($C_3$) and chromatic aberrations ($C_c$) of the cathode lens on the image side are well understood and given by: $C_c = -L\sqrt{\frac{E}{E_0}} + C_{cm}$ and $C_3 = L\sqrt{\frac{E}{E_0}} + C_{3m}$, where $L$ is the sample – objective distance (2-3 mm) and $C_{cm}$ and $C_{3m}$ are the chromatic and spherical aberrations of the magnetic part of the objective lens [30]. $E$ and $E_0$ are the electrons' landing energy and final energy after the acceleration. The first terms in $C_c$ and $C_3$ are electrostatic part

We experimentally measured these two aberration coefficients of the Elmitec AC-SPELEEM. For spherical aberration, we used the real-space LEED (RS-LEED) method, proposed by Prof. Rudolf Tromp [31]. In this method, a Si(111) surface is illuminated by a fine electron beam of 250-500 nm in size, and the diffracted beams in the Gaussian image plane are observed with slight defocusing. The displacements of these beams depend nonlinearly on the diffracted angles with the defocus and the 3rd-order spherical aberration as prefactors. The experimental spherical aberration coefficients of the microscope are in satisfactory agreement with the theoretical simulations (Figure 30). It is not possible to measure the chromatic aberration directly. By looking at the relationship between the excitation of the objective lens and the landing energy, $E$ in LEEM mode, we could obtain the electrostatic part. By adjusting $E_0$ in UVPEEM mode and quantifying the shift in focus, again in the unit of the excitation current of the objective lens, we could derive the magnetic part, along with the mirror contribution. Our findings suggest these two parts are almost equal with opposite signs, thus indicating the mirror effectively compensates for the chromatic aberration from the objective lens.

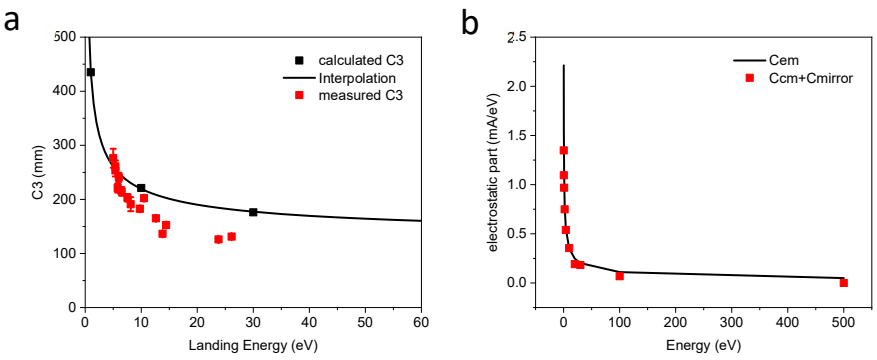


*Figure 30. MAXPEEM AC-SPELEEM spherical and chromatic aberrations. (a) Calculated spherical ($C_3$) aberration coefficient (black squares) at three different energies (1, 10, 30 eV), fitted with a 1/sqrt(E) interpolation (black line). Experimentally measured C3 (red squares) were obtained with real space micro-LEED. (b) Chromatic aberrations (indirect results in the unit of mA/eV) of the objective lens and the mirror. When the electrostatic part (solid black curve) and the magnetic part plus the mirror part (red squares) are equal but with opposite signs, the chromatic aberration of the objective lens is fully compensated by the mirror.*

In the case of XPEEM, it is crucial to keep the photon flux as low as possible to diminish the space charge effect. Space charge effects always occur when there is a very high electron density in the (photo)electron beam. It is frequently observed with microscopes installed at a synchrotron due to the pulsed nature of the photon source [32,33]. The space charge effect first occurs at the sample surface before the acceleration and then in the electron crossovers in the imaging column. Low photon flux at the sample, i.e., by detuning the undulator's gap, is the main factor in eliminating the space charge effect (*e.g.*, compare Figure 31a and b). When the aberration-corrector is ON, an extra space charge effect occurs in the mirror column, where electrons decelerate and the space charge effect there is even more severe than at the surface (*e.g.*, compared Figure 31b and c). To mitigate space charge effects in the microscope, especially in the mirror column, one has to decrease the electron beam flux inside the column. One way to do it is to introduce a field limiting aperture (selected area aperture, SAA) during image acquisition as seen in the comparison of Figure 31c and d (as well as Figure 31e and f with core-level photoelectrons). The drawback of putting SAA in the XPEEM mode is image vignetting if the sampling area is less than a field of view (FoV). For example, in Figure 31d (as well as Figure 31f), a 100 µm SAA was inserted to reduce the space charge, which in fact reduces the visible size of the image from the original FoV of 10 µm to 5 µm. In our microscope, we introduced another remedy to mitigate the space charge effect in the mirror column – a knife-limiting edge. This edge is installed in

the middle of the intermediate imaging column, which is close to a dispersive plane of the electron beam. It cuts secondary photoelectrons thus significantly improving the quality of core-level XPEEM images (*e.g.*, compare Figure 31e and g). Figure 31h demonstrates the enhanced action of both SAA and knife in the aberration-corrected XPEEM imaging mode. Using the corrector and limiting the electron beam in the microscope we easily get a moderate resolution of 50 nm with much higher transmission that scales with the opening of the contrast apertures (CA = 70 μm for the corrector ON compared with 30 μm for the corrector OFF case).

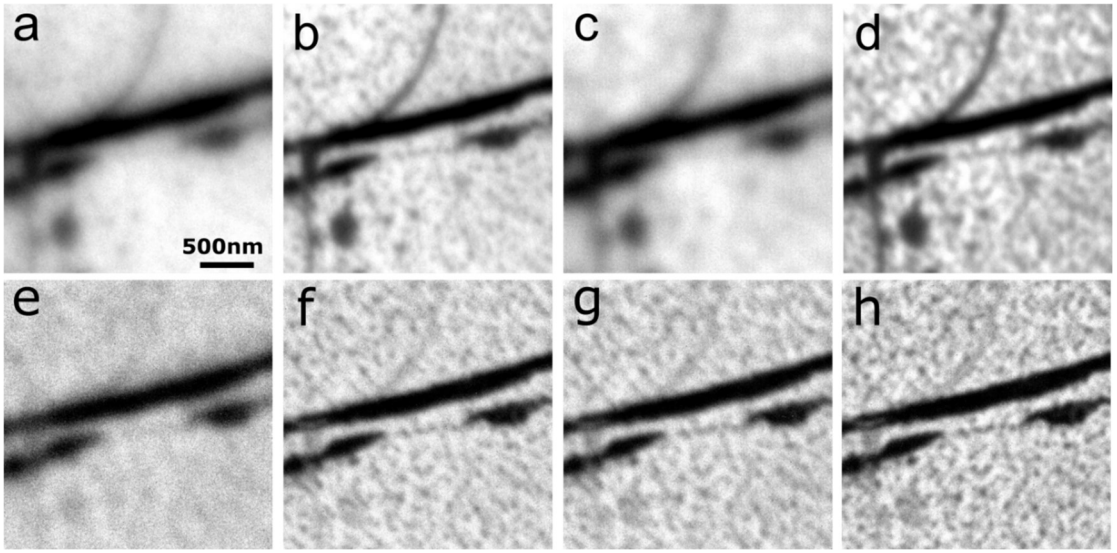


*Figure 31. The influence of different measurement conditions on the manifestation of space charge effects in XPEEM. Top row: secondary XPEEM images, (a) high photon flux of 4.2 ×10$^{13}$ ph/s, (b) low photon flux of 1.4 ×10$^{13}$ ph/s in the mirror-off mode, (c) same as (b) but in the mirror-on mode, (d) same as (c) with insertion of the SAA (100 μm). Lower row: Si2p core-level XPEEM images, (e) same as (c), (f) with SAA inserted, (g) with the knife aperture inserted (no SAA), and (h) with both SAA and the knife inserted. All presented XPEEM images are 2.5 × 2.5 μm$^2$, cropped from raw images with FoV = 10 μm. The sample is monolayer graphene with a few bilayer islands grown on SiC (0001). In the mirror-on (mirror-off) mode, the 70 μm (30 μm) CA was always used. The photon energy used for all images was 150 eV. The integration time of (a)-(d) was 3.2 s and for (e)-(h), it was 320 s.*

# 5 Points of concern

Current issues, areas where the beamline performance may not be optimal yet, or foreseeable risks to successful continuous operation, are summarized here. While some of these points of concern are not critical for day-to-day operation at present, awareness of their existence is essential for prioritizing development directions beyond current capabilities. Planned/proposed/potential developments to address the aforementioned issues are presented, and in more detail in Section 6 if needed.

User points of concern, derived from comments and grades in user feedback, include: (a) the lack of documentation (i.e. a master manual), (b) complex experimental operation, (c) complicated data access procedures (IT group responsibility), and (d) the lack of suitable data analysis tools. A master manual is currently under development; that should reduce operational complexity. Our purchase of several portable solid-state hard drives has enabled users to quickly copy data from beamline computers, thus alleviating the need for remote data access. Evangelos is developing Python- and Igor-based data analysis tools as described in Section 6.2. We note that the majority of users are satisfied with their overall experience (5 out of 5 rating), and scientific support by the beamline staff consistently receives the largest fraction of 5 out of 5 grades.

## 5.1 Beamline

Several concerns exist for the beamline: (a) spatial stability of the photon beam, (b) carbon contamination of the beamline elements, and (c) the lack of post-M4 characterization.

The heat load on the M1 beamline mirror is significant, especially when the undulator gap is small, and thermal deformation of M1 causes the beam to drift horizontally when the photon energy changes. Furthermore, for low photon energies below 40 eV, the heat load induces tiny mirror movements which results in a spatial shift of the beam. Unfortunately, the magnitude of the shift is comparable to the beam size (10 μm) and the timescale of the shift is 6-12 hours. This is problematic for overnight ARPES measurements that utilize low photon energies. We plan to mitigate these adverse effects by monitoring the beam at the exit slit (coated with phosphor) with a camera and implementing an M1 correction algorithm to automatically compensate for the shift.

We plan to perform oxygen cleaning of the beamline optical elements to address the carbon contamination issue.

To improve the quality of the X-ray absorption spectra, one needs to normalize the spectrum to a background. The beamline currently features a sub-optimal setup for i0-type normalization. A gold mesh is installed upstream of M4; it's dirty and we cannot deposit fresh gold onto it, hence the performance is sub-optimal. We intend to install a gold mesh for measuring photocurrent right before the beam impinges the sample, as described in Section 6.1.

## 5.2 Spectroscopic microscopy end station

Several concerns exist for the end station: (a) temperature stability while cooling the sample, (b) overall age of the microscope and its effect on ultimate performance, and (c) the lack of comprehensive documentation.

We use liquid nitrogen to cool samples and the lowest achievable temperature is 100 K. Three major limitations exist with the current setup. First, the sample cannot remain at the coldest temperature for more than ~4 hours without refilling the liquid nitrogen dewar. Second, temperature regulation is challenging; we can only regulate the nitrogen flow to set the temperature (no PID controller) hence thermal drifts during the experiment are omnipresent. Third, we cannot reach temperatures below 100 K, which is crucial for numerous magnetic material studies. One cooling solution is closed-cycle helium cooling for MAXPEEM, such as the "Stinger" system from Cold Edge Technologies. Closed cycle is preferred given current prices for liquid helium and the absence of a helium recycling system at MAX IV.

The age of the microscope is such that certain components (e.g. high-voltage electronics) need to be renewed, in order to enable the microscope to continue to operate at its ultimate performance level.

Work is in-progress on the beamline and end station manual; we expect a significant portion of the work to be completed during the summer shutdown of 2023.

### 5.3 General

A general point of concern is how to increase beamtime utilization. The MAXPEEM end station is a complex instrument that is challenging for inexperienced users to operate, due to the need for microscope lens alignment and the number of parameters to optimize during the measurement (for example, when switching modes). Support by the beamline staff is guaranteed for 12 hours during the day. Overnight beamtime utilization varies on a case-by-case basis. Magnetic material studies where users simply switch the beamline polarization and restart the measurement do partially/fully utilize overnight beamtime. Studies involving frequent mode-switching (imaging to μ-XPS to XPEEM to etc.) and multiple sample changes are challenging for users to perform overnight, hence overnight beamtime is rarely used in these cases.

We expect a gradual transition to greater user independence and overnight utilization of the instrument as our master manual evolves and software tools that assist users with microscope alignment and on-the-fly data analysis are rolled out.

## 6 Developments: ongoing, planned and possible

### 6.1 Beamline

Beamline developments include: (a) a new monochromator grating, (b) automatic M1 alignment and (c) photon flux normalization with a gold mesh in the column chamber.

We are currently using two monochromator gratings, a low-density (LD) grating with 300 l/mm and a high-density (HD) grating with 1221 l/mm. Technical details are found in Table 4 and delivered photon flux per grating is shown in Figure 7. The resolving power of the HD grating, at 400 eV, was measured to be 7000; the resolving power of the LD grating is three times lower. We will install a new 650 l/mm monochromator grating during the summer shutdowns and plan to operate mostly using this grating. The new grating will increase the resolving power at low energies (< 300 eV) and compensate for the

reduced flux of the beamline at energies higher than 500 eV. The efficiency curve of the new grating, as characterised at BESSY-II, is shown in Figure 32.

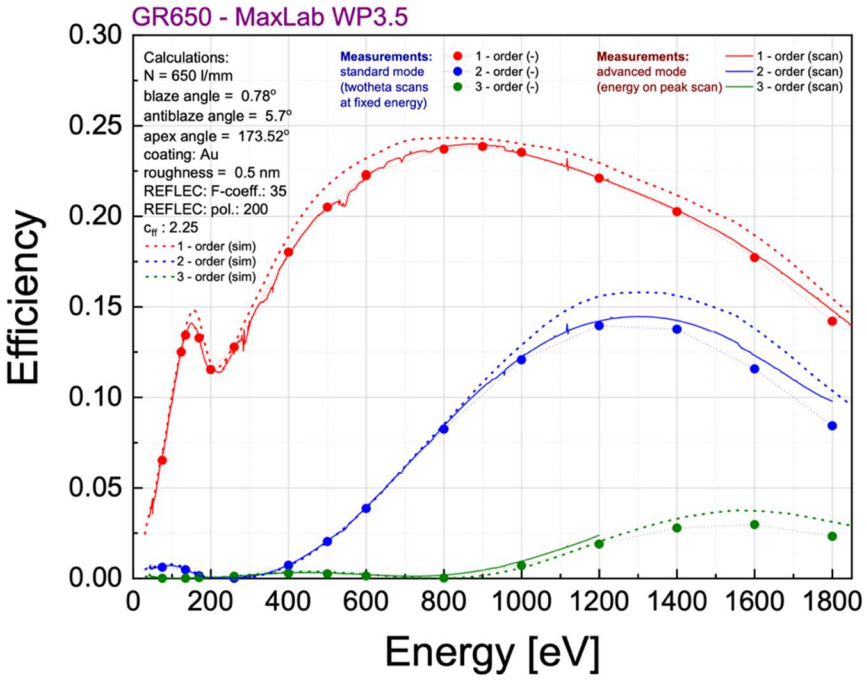


*Figure 32. Efficiency of the new 650 l/mm monochromator grating that will be installed during the summer shutdown of 2023. Solid and dashed lines represent measured and simulated values, respectively.*

To compensate for the M1-related beam shifts described in Section 5.1, we are planning to implement an M1 automatic correction algorithm as described earlier.

To normalize measured X-ray absorption spectra, we need to measure the photon flux right before the beam impinges the sample to remove absorption effects (e.g. carbon *K*-edge) originating from contaminated optical elements. The best place to measure the beamline flux is in the column chamber of the microscope, hence we are designing a flange (*Figure 33*) that will be mounted onto the column chamber. The flange will accommodate a small vacuum system, a gold mesh connected to an electrical feedthrough and a gold evaporator for refreshing the surface of the mesh. This system will enhance the accuracy of XAS measurements and potentially enable us to quantitatively measure XMC(L)D spectra by removing beamline-related absorption artefacts.

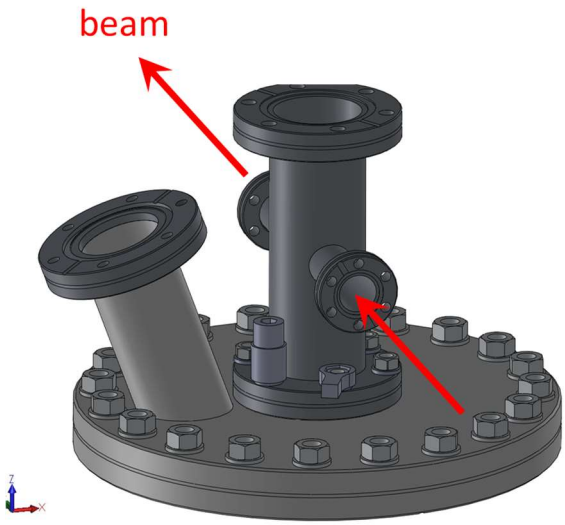


*Figure 33. Preliminary CAD drawing of a flange that will be mounted onto the column chamber of the microscope and hold the gold mesh (for i0 normalization) and titanium sublimation pump.*

## 6.2 Existing spectroscopic microscopy branch line

Spectroscopic microscopy end station developments include: (a) automatic alignment of the microscope, (b) motorization of the sample manipulator, (c) installation of a new analyser camera, (d) software development of data analysis tools, (e) the creation of a master beamline and end station operation manual and (f) beamline control improvements.

We are working with our colleagues in the MAX IV Scientific Software team to develop control software to automatically align the microscope, using an artificial intelligence algorithm. Successful automation of the microscope alignment process is an important step towards greater user independence and higher overnight beamtime utilization. Full motorization of the sample manipulator, described next, is coupled with the software development.

We have tasked Elmitec, the microscope manufacturer, with an upgrade project: to motorize the X and Y translation, and horizontal and vertical tilt functions of the manipulator. Post-motorization, we should be able to program a series of translations, automatically acquire images across the sample surface, and stitch them together to create a survey image; this will reduce the amount of human time needed to identify 2D material flakes on the surface of a silicon wafer, for example.

We have recently completed the procurement of a new state-of-the-art camera, the XF416(ES), from TVIPS GmbH, which will be installed in late summer 2023. The new camera is a 16-megapixel model that covers an image area of 63.5 x 63.5 mm². Its exceptional acquisition speed of up to 48 fps (at a resolution of 4k x 4k) is a vast improvement over our current camera's 5 fps, making it the best choice for our AC-SPELEEM. Furthermore, it is compatible with our current UHV setups and software environments.

The availability of easy-to-use and on-the-fly data analysis tools is known to improve beamtime productivity, both during the beamtime and afterwards. The primary image analysis tool that was

used, until recently, at MAXPEEM is ImageJ, an open-source project with a plethora of plugins to help users perform various image processing tasks. In-house developed data analysis packages, written in Python and for Igor Pro, are now available. Early versions of the software have already been adopted by users, and development is ongoing.

Python: Users can launch Jupyter notebooks, with MAXPEEM specific add-on packages, on MAX IV servers. The launch menu is shown in Figure 34. The in-house developed package py4uview allows one to load experimental data from MAXPEEM, and packs the images and microscope metadata into a single file. Other packages that offer tools for image viewing, processing, and analysis (opencv, scipy, numpy and others) are loaded with the notebooks.

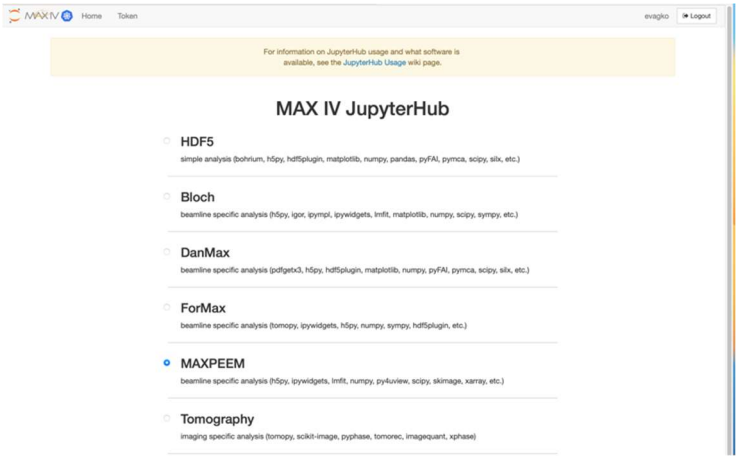


*Figure 34. Launch menu for the MAXPEEM Jupyter notebook*

Igor Pro: We have publicly released a beta version of the MAXPEEM data analysis package for our users on gitlab. A screenshot of the analysis package is shown in Figure 35. The package allows users to quickly interact with their data for surveying and perform deep analysis, leveraging all of the capabilities of Igor Pro. We have developed functions and macros for handling data recorded with different microscope operation modes: LEED; LEEM; (X)PEEM; XPS; ARPES and XAS. The enrichment and expansion of the package capabilities continues, motivated by users' feedback.

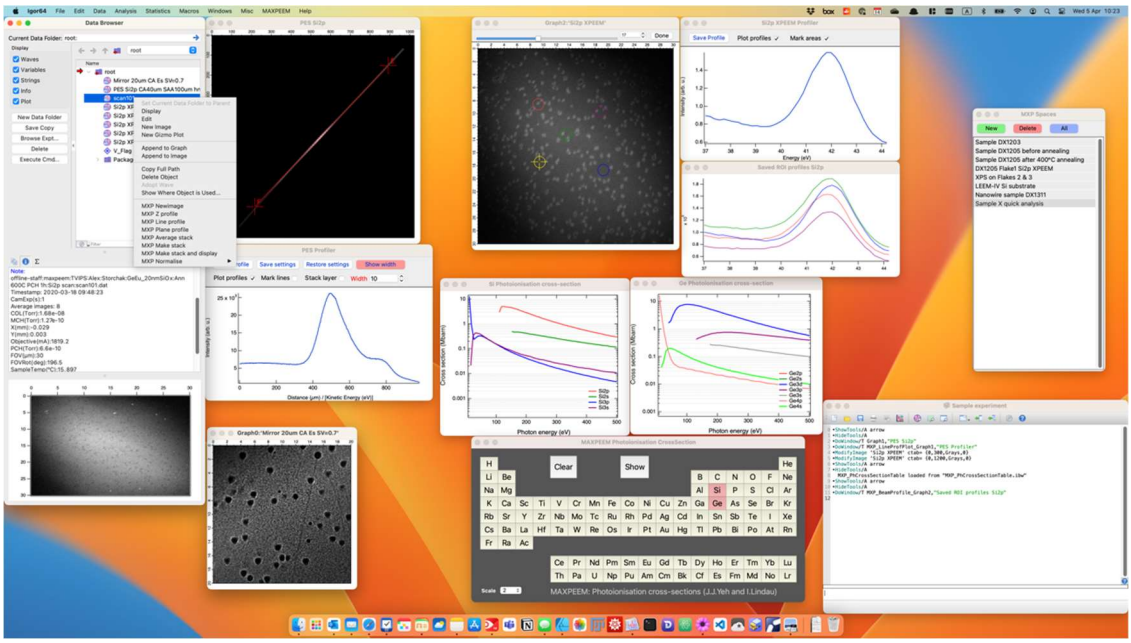

*Figure 35. Screenshot of Igor Pro running on macOS, featuring various analysis tools from the in-house developed MAXPEEM data analysis package.*

Development of a master operation manual for the end station, beamline, microscope, and software will start during the summer shut down; our aim is to make the full manual available to users by the end of 2023.

Improvements in beamline control are ongoing. One project targets the magnetic materials research community. At present, we rotate the light polarisation plane (inclined mode of the undulator) manually by setting the undulator's gap and phase. Figure 36 shows a graphical representation of a lookup table we used for the study of antiferromagnetic hematite (iron oxide).

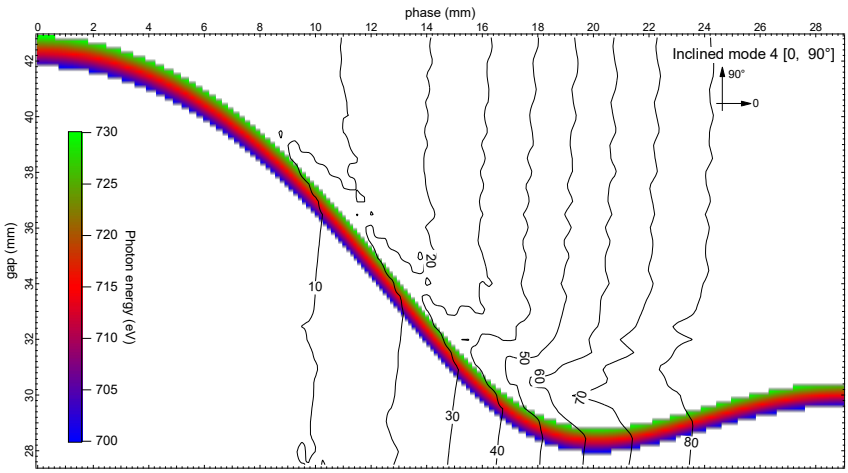


*Figure 36. Graphical representation of a lookup table relevant for iron L-edge measurements. It maps photon energy and angle to undulator gap and phase.*

We have calculated our undulator's spectra in inclined modes and experimentally verified our predictions using an x-ray polarimeter. We plan to add new lookup tables for all angles and energies above 500 eV (relevant for the most common magnetic metal *L*-edges) to our beamline control

system. Users will simply input the desired polarization angle and photon energy and the control system will set the corresponding undulator values in the background. This development, combined with already implemented software developments (e.g. one-click XMCD/XMLD spectra acquisition) should enable users to be more productive.

## 6.3 Plans for a second branch line

It is possible to build another branch line from the MAXPEEM port that would have its own M3, exit slit, refocusing mirror(s) and end station. The primary branch and associated upgrades have been our focus up until now. With the recent upgrades in place or coming in place during 2023, attention can shift to the conceptualization and design of the second branch. We have two proposals at present for the second branch end station: near ambient pressure PEEM (NAP-PEEM) and NanoESCA with a spin filter (spin-KPEEM). The proposals are at the conceptualization stage and further work is needed to gauge user interest and science cases, solicit financing and perform a detailed optical design.

### *6.3.1* Near ambient pressure-PEEM

Near Ambient Pressure Photoemission Electron Microscopy (NAP-PEEM) is a powerful imaging technique that enables direct observation of the chemical and physical properties of surfaces at near-ambient pressures (typically ranging from $10^{-3}$ to $10^{-1}$ mbar). This technique combines the capabilities of photoemission spectroscopy (PES) and microscopy and provides detailed information on the electronic structure and chemical composition of surfaces under realistic conditions, such as those encountered in catalytic reactions, gas-surface interactions, and electrochemical processes.

The most important advantage of NAP-PEEM is that it can be used to study materials in their native environment, without the need for ultra-high vacuum conditions. This is particularly useful for studying catalytic reactions, where the presence of gases can significantly affect the properties of the surface. If implemented, NAP-PEEM at MAXPEEM could be very attractive to industry (e.g. metal corrosion, catalysis), especially since UHV-based PEEM at MAXPEEM has already generated results of interest for the metals industry in Sweden. Furthermore, the implementation of a NAP-PEEM second branch enables us to physically separate the beamline for fundamental and industrial research (ie. UHV-based PEEM for surface science, 2D magnetic materials research, etc., NAP-PEEM for steel alloy corrosion, catalysis, etc. research). One could expect improved beamline throughput (e.g. less time spent switching the setup between surface science vs. metal corrosion studies) and uptime from such a scheme.

Both Elmitec and SPECS have developed their own NAP-PEEM/LEEM instrument [29,34,35]. A SPECS NAP-PEEM instrument has been installed at the Dalian Institute of Chemical Physics (Chinese Academy of Sciences) with a tunable deep ultraviolet laser source. Elmitec has installed a NAP-LEEM at Leibniz Universität (Hannover, Germany). To the best of our knowledge, no NAP-PEEM/LEEM has been installed at a synchrotron facility at present. However, some users have expressed interest in using such an instrument to investigate catalysts and corrosion of industrially-relevant metals.

We note that other beamlines at MAX IV, such as HIPPIE, have expressed interest in scanning NAP-PEEM.

### *6.3.2* k-PEEM (nano ESCA with spin filter)

Momentum Photoemission Electron Microscopy (k-PEEM) has gained considerable attention in recent times, primarily due to the surge of interest in the band structures of two-dimensional (2D) materials since the discovery of graphene. Similar to a standard PEEM, k-PEEM offers real-space imaging capabilities; however, it especially shines in its enhanced proficiency in k-space - conducting μ-ARPES with improved energy resolution. Various k-PEEM models are commercially available, but for the purpose of this discussion we will focus on the Nano ESCA model from Focus GmbH, illustrating its potential if integrated as the end station of the second branch line of MAXPEEM [36].

The Nano ESCA distinguishes itself through its unique design featuring double hemispherical analyzers [37]. The second analyzer is ingeniously structured symmetrically to offset the aberrations introduced by the first analyzer. By manipulating the intermediate lenses nestled between the two analyzers, they can function collectively as a full-spherical analyzer. This design leads to a doubling of the energy dispersion and consequently enhances the energy resolution.

In the Nano ESCA, the electron energy within the analyzer is properly reduced, enabling the analyzer's pass energy to be set at a low value, like that of a conventional ARPES instrument. This adjustment yields an impressive energy resolution of 12 meV. By using an iris aperture, similar to the selected area aperture in AC-SPELEEM, it becomes possible to perform μ-ARPES on an area smaller than 6 μm. Notably, this k-PEEM also serves imaging applications, boasting a spatial resolution of less than 40 nm. For instance, when synchrotron light is incident at a grazing angle, XMCD images can be captured from a sample with in-plane magnetization, complementing the existing AC-SPELEEM that is only capable of measuring out-of-plane magnetization. It's important to note that NAP-PEEM also possesses this ability when the synchrotron light is incident at a grazing angle.

One significant advantage of Nano ESCA is the potential integration of a 2D imaging spin filter, enabling k-PEEM to be spin-resolved in both real and momentum spaces [38]. In this spin filter, an image is projected onto a gold/iridium crystal where, due to spin-orbit coupling, one spin polarization is preferred, resulting in a spin-filtered reflection. The crystal is optimized for high spin-sensitivity and reflectivity. This process enhances the figure-of-merit by utilizing multiple parallel detection channels.

In conclusion, k-PEEM has the potential to meet the requirements of a variety of experiments necessitating high-resolution μ-ARPES from small areas, while maintaining the capability for real-space imaging. This is a feat that the current AC-SPELEEM and ARPES at the Bloch beamline have not yet achieved.

### *6.3.3* Open port for mobile end stations

The second branch line can be established as an open port for connecting mobile end stations. This solution requires the installation of only a few optical elements, simplifying the setup process. The design of this branch line should prioritize versatility and accommodate diverse instruments from various users. For example, a potential candidate for this setup is the current Scanning Transmission X-ray Microscopy (STXM) end station at SoftiMAX. If relocated to MAXPEEM, this instrument could measure the *K*-edges of sulfur (S) and carbon (C), a capability currently unattainable at the 3 GeV ring.

Additionally, the port at the second branch line could serve as an invaluable testing platform for the development and fine-tuning of new instruments and end stations.

## 6.4 Other developments projects

MAXPEEM is well-positioned to investigate heterostructure stacks of 2D materials, a field that has gained widespread interest in the condensed matter physics community, since the stacks are typically fabricated from µm-sized exfoliated flakes [14,39–41]. Such stacks offer one approach to materials by design; one aims for combined or even new properties by combining different 2D materials. Lately, we have observed increased interest from user groups, via their submitted proposals, regarding these material systems. Sample degradation due to air exposure is a substantial concern for these user groups and the lack of suitable systems for handling these materials is expected to discourage other users from applying for beamtime.

One planned development is in the area of sample preparation and environment. To facilitate their study, a transfer stage for heterostructure stacking and manipulation (e.g. commercial system from https://www.hq2d.com) is required. A fully motorized system, operating in an argon glovebox, should yield high quality samples for measurement. Once the samples have been prepared, our (already available) in-house developed vacuum suitcase enables direct transfer of the sample from the glovebox into the vacuum system without air exposure.

# 7 Appendix

## 7.1 Summary of user feedback in table form

| | Year | Area | Number of instances |
|---|---|---|---|
| **5 out of 5 rating** | *2023* | **Total surveys collected** | **2** |
| | | Final grade | 1 |
| | | Scientific support by staff | 1 |
| | | Beamline data processing and software | -- |
| | | Beamline experiment control | 2 |
| | | Beamline equipment: endstation, sample env, .. | 1 |
| | | Beamline documentation | 1 |
| | | IT services | 1 |
| | *2022* | **Total surveys collected** | **34** |
| | | Final grade | 17 |
| | | Scientific support by staff | 28 |
| | | Beamline data processing and software | 15 |
| | | Beamline experiment control | 15 |
| | | Beamline equipment: endstation, sample env, .. | 15 |
| | | Beamline documentation | 10 |
| | | IT services | 15 |
| | *2021* | **Total surveys collected** | **10** |
| | | Final grade | 6 |
| | | Scientific support by staff | 10 |
| | | Beamline data processing and software | 4 |

| | | | |
|---|---|---|---|
| | | Beamline experiment control | 4 |
| | | Beamline equipment: endstation, sample env, .. | 7 |
| | | Beamline documentation | 3 |
| | *2020* | **Total surveys collected** | **12** |
| | | Final grade | 6 |
| | | Scientific support by staff | 9 |
| | | Beamline data processing and software | 7 |
| | | Beamline experiment control | 6 |
| | | Beamline equipment: endstation, sample env, .. | 9 |
| | | Beamline documentation | 6 |
| | *2019* | **Total surveys collected** | **8** |
| | | Final grade | 4 |
| | | Scientific support by staff | 7 |
| | | Beamline data processing and software | 3 |
| | | Beamline experiment control | 4 |
| | | Beamline equipment: endstation, sample env, .. | 4 |
| | *2018* | **Total surveys collected** | **1** |
| | | Final grade | 1 |
| | | Scientific support by staff | 1 |
| | | Beamline data processing and software | 1 |
| | | Beamline experiment control | 1 |
| | | Beamline equipment: endstation, sample env, .. | 1 |
| **3/2/1, out of 5 rating** | *2023* | Final grade | 1 |
| | *2022* | Beamline documentation | 6 |
| | | Beamline data processing and software | 3 |
| | | Beamline experiment control | 2 |
| | | Beamline equipment: endstation, … | 4 |
| | | Lab facilities | 2 |
| | | IT services | 3 |
| | | Common areas | 2 |
| | *2021* | Beamline documentation | 1 |
| | | IT services | 2 |
| | | Beamline data processing | 1 |
| | *2020* | Final grade | 1 |
| | | Beamline documentation | 3 |
| | | Lab facilities | 2 |
| | | Beamline experiment control | 1 |
| | | Beamline data processing | 1 |
| | | IT services | 4 |
| | | Delivered beam | 1 |
| | *2019* | Final grade | 1 |
| | | Beamline documentation | 2 |
| | | Common areas: lunch room | 2 |
| | | Safety information and procedures | 1 |
| | | Lab facilities: chemistry lab, etc. | 2 |
| | | Beamline data processing and software | 2 |
| | | IT services | 1 |
| | | Delivered beam: machine operation, etc. | 1 |
| | *2018* | --- | --- |

## 7.2 MAXPEEM publication list


1. Wang, Y. *et al.* Polaronic Trions Induced by Strong Interfacial Coupling in Monolayer WSe2. *Adv. Electron. Mater.* **9**, 2200852 (2023).
2. Talebi, P., Rani, E., Niu, Y., Zakharov, A. & Cao, W. Spectromicroscopic determinations of chemical environments of Ni in MoS2-Ag-Ni ternary systems. *X-Ray Spectrom.* **52**, 38–45 (2023).
3. Liang, M. *et al.* Spatially Resolved Local Electronic Properties of 2D Lead Halide Perovskite Single Crystals Studied by X-Ray Photoemission Electron Microscopy. *Sol. RRL* **7**, 2200795 (2023).
4. Niu, Y. *et al.* MAXPEEM: a spectromicroscopy beamline at MAX IV laboratory. *J. Synchrotron Radiat.* **30**, 1–11 (2023).
5. Reimers, S. *et al.* Current-driven writing process in antiferromagnetic Mn2Au for memory applications. *Nat. Commun.* **14**, 1861 (2023).
6. Polley, C. M. *et al.* Bottom-Up Growth of Monolayer Honeycomb SiC. *Phys. Rev. Lett.* **130**, 076203 (2023).
7. Shtepliuk, I. *et al.* Understanding of the Electrochemical Behavior of Lithium at Bilayer-Patched Epitaxial Graphene/4H-SiC. *Nanomaterials* **12**, 2229 (2022).
8. Karakachian, H. *et al.* Periodic Nanoarray of Graphene pn-Junctions on Silicon Carbide Obtained by Hydrogen Intercalation. *Adv. Funct. Mater.* **32**, 2109839 (2022).
9. Zhu, L. *et al.* Surface chemistry and diffusion of trace and alloying elements during in vacuum thermal deoxidation of stainless steel. *Surf. Interface Anal.* **54**, 99–108 (2022).
10. Neckel, I. T. *et al.* Unveiling Center-Type Topological Defects on Rosettes of Lead Zirconate Titanate Associated to Oxygen Vacancies. *Ann. Phys.* **534**, 2100219 (2022).
11. Singh, H. *et al.* Unveiling nano-scaled chemical inhomogeneity impacts on corrosion of Ce-modified 2507 super-duplex stainless steels. *npj Mater. Degrad.* **6**, 54 (2022).
12. Rani, E. *et al.* Unraveling compensation between electron transfer and strain in Ni-Ag-MoS2 photocatalyst. *J. Catal.* **414**, 199–208 (2022).
13. Mousavi, S. F. *et al.* Atomic Hydrogen Annealing of Graphene on InAs Surfaces and Nanowires: Interface and Morphology Control for Optoelectronics and Quantum Technologies. *ACS Appl. Nano Mater.* **5**, 17919–17927 (2022).
14. Lin, W. *et al.* Combining two-photon photoemission and transient absorption spectroscopy to resolve hot carrier cooling in 2D perovskite single crystals: the effect of surface layer. *J. Mater. Chem. C* **10**, 16751–16760 (2022).
15. Rani, E. *et al.* Uncovering temperature-tempted coordination of inclusions within ultra-high-strength-steel via in-situ spectro-microscopy. *J. Mater. Res. Technol.* **17**, 2333–2342 (2022).
16. Armakavicius, N. *et al.* Resolving mobility anisotropy in quasi-free-standing epitaxial graphene by terahertz optical Hall effect. *Carbon N. Y.* **172**, 248–259 (2021).
17. Selegård, L., Skallberg, A., Zakharov, A., Abrikossova, N. & Uvdal, K. Step by step rare-earth catalyzed SiOx annealing and simultaneous formation of Europium- silicide by low coverage of Eu doped Gd2O3 nanoparticles. *Surf. Sci.* **704**, 121743 (2021).
18. Singh, H. *et al.* Unveiling interactions of non-metallic inclusions within advanced ultra-high-strength steel: A spectro-microscopic determination and first-principles elucidation. *Scr. Mater.* **197**, 113791 (2021).

19. Bokai, K. A. *et al.* Visualization of graphene grain boundaries through oxygen intercalation. *Appl. Surf. Sci.* **565**, 150476 (2021).

20. Boix, V. *et al.* Area-selective Electron-beam induced deposition of Amorphous-BNx on graphene. *Appl. Surf. Sci.* **557**, 149806 (2021).

21. Bouhafs, C. *et al.* Synthesis of large-area rhombohedral few-layer graphene by chemical vapor deposition on copper. *Carbon N. Y.* **177**, 282–290 (2021).

22. Wang, C. *et al.* Highly dispersed Cu atoms in MOF-derived N-doped porous carbon inducing Pt loads for superior oxygen reduction and hydrogen evolution. *Chem. Eng. J.* **426**, 130749 (2021).

23. Bommanaboyena, S. P. *et al.* Readout of an antiferromagnetic spintronics system by strong exchange coupling of Mn2Au and Permalloy. *Nat. Commun.* **12**, 6539 (2021).

24. Zakharov, A. A. Ambipolar Behavior of Ge-Intercalated Graphene: Interfacial Dynamics and Possible Applications. *Front. Phys.* **9**, (2021).

25. Stanishev, V. *et al.* Critical View on Buffer Layer Formation and Monolayer Graphene Properties in High-Temperature Sublimation. *Appl. Sci.* **11**, 1891 (2021).

26. Nguyen, T. T. N. *et al.* Topological Surface State in Epitaxial Zigzag Graphene Nanoribbons. *Nano Lett.* **21**, 2876–2882 (2021).

27. Shi, Y. *et al.* Epitaxial Graphene Growth on the Step-Structured Surface of Off-Axis C-Face 3C-SiC($1^{-}1^{-}1^{-}$). *Phys. status solidi* **257**, 1900718 (2020).

28. Li, H. *et al.* Atomic-Scale Tuning of Graphene/Cubic SiC Schottky Junction for Stable Low-Bias Photoelectrochemical Solar-to-Fuel Conversion. *ACS Nano* **14**, 4905–4915 (2020).

29. Kim, K. H. *et al.* Chemical Sensing with Atomically Thin Platinum Templated by a 2D Insulator. *Adv. Mater. Interfaces* **7**, 1902104 (2020).

30. Momeni Pakdehi, D. *et al.* Silicon Carbide Stacking-Order-Induced Doping Variation in Epitaxial Graphene. *Adv. Funct. Mater.* **30**, 2004695 (2020).

31. Forti, S. *et al.* Semiconductor to metal transition in two-dimensional gold and its van der Waals heterostack with graphene. *Nat. Commun.* **11**, 2236 (2020).

32. Aprojanz, J. *et al.* High-Mobility Epitaxial Graphene on Ge/Si(100) Substrates. *ACS Appl. Mater. Interfaces* **12**, 43065–43072 (2020).

33. Kim, K. H. *et al.* Ambipolar charge transport in quasi-free-standing monolayer graphene on SiC obtained by gold intercalation. *Phys. Rev. B* **102**, 165403 (2020).

34. Karakachian, H. *et al.* One-dimensional confinement and width-dependent bandgap formation in epitaxial graphene nanoribbons. *Nat. Commun.* **11**, 6380 (2020).

35. Shi, Y. *et al.* A patterning-free approach for growth of free-standing graphene nanoribbons using step-bunched facets of off-oriented 4H-SiC(0 0 0 1) epilayers. *J. Phys. D. Appl. Phys.* **53**, 115102 (2020).

36. Rullik, L. *et al.* Surface oxide development on aluminum alloy 6063 during heat treatment. *Surf. Interface Anal.* **51**, 1214–1224 (2019).

37. Aprojanz, J., Bampoulis, P., Zakharov, A. A., Zandvliet, H. J. W. & Tegenkamp, C. Nanoscale imaging of electric pathways in epitaxial graphene nanoribbons. *Nano Res.* **12**, 1697–1702 (2019).

38. Zakharov, A. A. *et al.* Wafer Scale Growth and Characterization of Edge Specific Graphene Nanoribbons for Nanoelectronics. *ACS Appl. Nano Mater.* **2**, 156–162 (2019).

39. Yazdi, G. R. *et al.* Effect of epitaxial graphene morphology on adsorption of ambient species. *Appl. Surf. Sci.* **486**, 239–248 (2019).

40. Link, S. *et al.* Introducing strong correlation effects into graphene by gadolinium intercalation. *Phys. Rev. B* **100**, 121407 (2019).

41. Scardamaglia, M. *et al.* Highlighting the Dynamics of Graphene Protection toward the Oxidation of Copper Under Operando Conditions. *ACS Appl. Mater. Interfaces* **11**, 29448–29457 (2019).

42. Ali-Löytty, H. *et al.* The role of (FeCrSi)2(MoNb)-type Laves phase on the formation of Mn-rich protective oxide scale on ferritic stainless steel. *Corros. Sci.* **132**, 214–222 (2018).

43. Aprojanz, J. *et al.* Ballistic tracks in graphene nanoribbons. *Nat. Commun.* **9**, 4426 (2018).

44. Laverock, J. *et al.* Observation of Weakened V—V Dimers in the Monoclinic Metallic Phase of Strained VO2. *Phys. Rev. Lett.* **121**, 256403 (2018).

45. Wang, W. *et al.* Flat-Band Electronic Structure and Interlayer Spacing Influence in Rhombohedral Four-Layer Graphene. *Nano Lett.* **18**, 5862–5866 (2018).

46. Shi, Y. *et al.* Elimination of step bunching in the growth of large-area monolayer and multilayer graphene on off-axis 3C SiC (111). *Carbon* **140**, 533–542 (2018).

47. Shi, X. *et al.* Quantification of Bonded Ni Atoms for M-M0S2 Metallic Contact through X-ray Photoemission Electron Microscopy. *Microsc. Microanal.* **24**, 458–459 (2018).

48. Shi, X. *et al.* Metallic Contact between MoS 2 and Ni via Au Nanoglue. *Small* **14**, 1704526 (2018).

49. Bouhafs, C. *et al.* Multi-scale investigation of interface properties, stacking order and decoupling of few layer graphene on C-face 4H-SiC. *Carbon N. Y.* **116**, 722–732 (2017).

50. Niu, Y. R., Zakharov, A. A. & Yakimova, R. Metal-dielectric transition in Sn-intercalated graphene on SiC(0001). Ultramicroscopy **183**, 49–54 (2017).

## 7.3 References

1. Niu, Y. *et al.* MAXPEEM: a spectromicroscopy beamline at MAX IV laboratory. *J. Synchrotron Radiat.* **30**, 1–11 (2023).

2. Nyholm, R., Andersen, J. N., Johansson, U., Jensen, B. N. & Lindau, I. Beamline I311 at MAX-LAB: a VUV/soft X-ray undulator beamline for high resolution electron spectroscopy. *Nucl. Instruments Methods Phys. Res. Sect. A Accel. Spectrometers, Detect. Assoc. Equip.* **467–468**, 520–524 (2001).

3. Klementiev, K. & Chernikov, R. Powerful scriptable ray tracing package xrt. in (eds. Sanchez del Rio, M. & Chubar, O.) 92090A (2014). doi:10.1117/12.2061400

4. Zakharov, A., Preobrajenski, A. & Sankari, R. *MaxPEEM beamline (1.5 GeV ring at MAX IV) Detailed Design Report*. (2014).

5. Leemann, S. C. Recent progress on the MAX IV 1.5 GeV storage ring lattice and optics. *IPAC 2012 - Int. Part. Accel. Conf. 2012* 1662–1664 (2012).

6. Sasaki, S. *et al.* Design of a new type of planar undulator for generating variably polarized radiation. *Nucl. Instruments Methods Phys. Res. Sect. A Accel. Spectrometers, Detect. Assoc. Equip.* **331**, 763–767 (1993).

7. Tanaka, T. & Kitamura, H. SPECTRA : a synchrotron radiation calculation code. *J. Synchrotron*

*Radiat.* **8**, 1221–1228 (2001).

8. Chubar, O., Elleaume, P. & Chavanne, J. A three-dimensional magnetostatics computer code for insertion devices. *J. Synchrotron Radiat.* **5**, 481–484 (1998).
9. Tanaka, T. Major upgrade of the synchrotron radiation calculation code SPECTRA. *J. Synchrotron Radiat.* **28**, 1267–1272 (2021).
10. Chen, C. T. & Sette, F. Performance of the Dragon soft x-ray beamline (invited). *Rev. Sci. Instrum.* **60**, 1616–1621 (1989).
11. Proceedings of the Fifth International Conference on LEEM/PEEM. in (eds. Altman, M. & Watanabe, Y.) (2006).
12. Moldovan, G., Matheson, J., Derbyshire, G. & Kirkland, A. Characterisation of a detector based on microchannel plates for electrons in the energy range 10–20keV. *Nucl. Instruments Methods Phys. Res. Sect. A Accel. Spectrometers, Detect. Assoc. Equip.* **596**, 402–408 (2008).
13. Zakharov, A. A. Ambipolar Behavior of Ge-Intercalated Graphene: Interfacial Dynamics and Possible Applications. *Front. Phys.* **9**, (2021).
14. Novoselov, K. S., Mishchenko, A., Carvalho, A. & Castro Neto, A. H. 2D materials and van der Waals heterostructures. *Science (80-. ).* **353**, (2016).
15. Li, L. *et al.* Black phosphorus field-effect transistors. *Nat. Nanotechnol.* **9**, 372–377 (2014).
16. Golias, E., Krivenkov, M., Varykhalov, A., Sánchez-Barriga, J. & Rader, O. Band Renormalization of Blue Phosphorus on Au(111). *Nano Lett.* **18**, 6672–6678 (2018).
17. Watts, M. C. *et al.* Production of phosphorene nanoribbons. *Nature* **568**, 216–220 (2019).
18. Yang, G., Xu, S., Zhang, W., Ma, T. & Wu, C. Room-temperature magnetism on the zigzag edges of phosphorene nanoribbons. *Phys. Rev. B* **94**, 075106 (2016).
19. Krivenkov, M. *et al.* One-dimensional electronic structure of phosphorene chains. *arXiv:2304.13456* (2023).
20. Bürckstümmer, H. *et al.* Efficient Solution-Processed Bulk Heterojunction Solar Cells by Antiparallel Supramolecular Arrangement of Dipolar Donor-Acceptor Dyes. *Angew. Chemie* **123**, 11832–11836 (2011).
21. Zhu, L. *et al.* Single-junction organic solar cells with over 19% efficiency enabled by a refined double-fibril network morphology. *Nat. Mater.* **21**, 656–663 (2022).
22. National Renewable Energy Laboratory. Best Research-Cell Efficiency Chart. *Best Research-Cell Efficiency Chart* (2023).
23. Hlawacek, G., Khokhar, F. S., van Gastel, R., Poelsema, B. & Teichert, C. Smooth Growth of Organic Semiconductor Films on Graphene for High-Efficiency Electronics. *Nano Lett.* **11**, 333–337 (2011).
24. Futscher, M. H. & Ehrler, B. Efficiency Limit of Perovskite/Si Tandem Solar Cells. *ACS Energy Lett.* **1**, 863–868 (2016).
25. Brennan, M. C., Ruth, A., Kamat, P. V & Kuno, M. Photoinduced Anion Segregation in Mixed Halide Perovskites. *Trends Chem.* **2**, 282–301 (2020).
26. Schulz, P., Cahen, D. & Kahn, A. Halide Perovskites: Is It All about the Interfaces? *Chem. Rev.* **119**, 3349–3417 (2019).
27. Man, G. J. *et al.* Electronic coupling between the unoccupied states of the organic and inorganic sublattices of methylammonium lead iodide: A hybrid organic-inorganic perovskite single crystal. *Phys. Rev. B* **104**, L041302 (2021).
28. García-Fernández, A. *et al.* Experimental and Theoretical Core Level and Valence Band Analysis

of Clean Perovskite Single Crystal Surfaces. *Small* **18**, 2106450 (2022).

29. Ning, Y. *et al.* A near ambient pressure photoemission electron microscope (NAP-PEEM). *Ultramicroscopy* **200**, 105–110 (2019).
30. Tromp, R. M. Measuring and correcting aberrations of a cathode objective lens. *Ultramicroscopy* **111**, 273–281 (2011).
31. Tromp, R. M. Characterization of the cathode objective lens by Real-Space Microspot Low Energy Electron Diffraction. *Ultramicroscopy* **130**, 2–6 (2013).
32. Schmidt, T., Sala, A., Marchetto, H., Umbach, E. & Freund, H.-J. First experimental proof for aberration correction in XPEEM: Resolution, transmission enhancement, and limitation by space charge effects. *Ultramicroscopy* **126**, 23–32 (2013).
33. Locatelli, A., Menteş, T. O., Niño, M. Á. & Bauer, E. Image blur and energy broadening effects in XPEEM. *Ultramicroscopy* **111**, 1447–1454 (2011).
34. Franz, T. *et al.* Catalytic CO oxidation on Pt under near ambient pressure: A NAP-LEEM study. *Ultramicroscopy* **200**, 73–78 (2019).
35. Ning, Y. *et al.* Tunable deep ultraviolet laser based near ambient pressure photoemission electron microscope for surface imaging in the millibar regime. *Rev. Sci. Instrum.* **91**, 113704 (2020).
36. FOCUS. NanoESCA MARIS. 1 Available at: https://www.focus-gmbh.com/nanoesca-maris/. (Accessed: 2nd June 2023)
37. Escher, M. *et al.* Nanoelectron spectroscopy for chemical analysis: a novel energy filter for imaging x-ray photoemission spectroscopy. *J. Phys. Condens. Matter* **17**, S1329–S1338 (2005).
38. Tusche, C., Krasyuk, A. & Kirschner, J. Spin resolved bandstructure imaging with a high resolution momentum microscope. *Ultramicroscopy* **159**, 520–529 (2015).
39. Balents, L., Dean, C. R., Efetov, D. K. & Young, A. F. Superconductivity and strong correlations in moiré flat bands. *Nat. Phys.* **16**, 725–733 (2020).
40. Basov, D. N., Averitt, R. D. & Hsieh, D. Towards properties on demand in quantum materials. *Nat. Mater.* **16**, 1077–1088 (2017).
41. Kennes, D. M. *et al.* Moiré heterostructures as a condensed-matter quantum simulator. *Nat. Phys.* **17**, 155–163 (2021).